

# Haumea's thermal emission revisited in the light of the occultation results

T. Müller<sup>a</sup>, Cs. Kiss<sup>b</sup>, V. Alí-Lagoa<sup>a</sup>, J. L. Ortiz<sup>c</sup>, E. Lellouch<sup>d</sup>, P. Santos-Sanz<sup>c</sup>, S. Fornasier<sup>d</sup>, G. Marton<sup>b</sup>, M. Mommert<sup>e</sup>, A. Farkas-Takács<sup>b,g</sup>, A. Thirouin<sup>e</sup>, E. Vilenius<sup>f</sup>

<sup>a</sup>Max-Planck-Institut für extraterrestrische Physik, Giessenbachstrasse 1, 85748 Garching, Germany

<sup>b</sup>Konkoly Observatory, Research Centre for Astronomy and Earth Sciences, Hungarian Academy of Sciences, H-1121 Budapest, Konkoly Thege Miklós út 15-17, Hungary

<sup>c</sup>Departamento de Sistema Solar, Instituto de Astrofísica de Andalucía (CSIC), Glorieta de la Astronomía s/n, 18008 Granada, Spain

<sup>d</sup>LESIA-Observatoire de Paris, CNRS, UPMC Univ. Paris 06, Univ. Paris-Diderot, France

<sup>e</sup>Lowell Observatory, 1400 W Mars Hill Rd, 86001, Flagstaff, Arizona, USA

<sup>f</sup>Max-Planck-Institut für Sonnensystemforschung, Justus-von-Liebig-Weg 3, 37077 Göttingen, Germany

<sup>g</sup>Eötvös Loránd University, Pázmány Péter s. 1/A, H-1171 Budapest, Hungary

---

## Abstract

A recent multi-chord occultation measurement of the dwarf planet (136108) Haumea (Ortiz et al. 2017) revealed an elongated shape with the longest axis comparable to Pluto's mean diameter. The chords also indicate a ring around Haumea's equatorial plane, where its largest moon, Hi'iaka, is also located. The Haumea occultation size estimate (size of an equal-volume sphere<sup>1</sup>  $D_{\text{equ}} = 1595$  km) is larger than previous radiometric solutions (equivalent sizes in the range between 1150 and 1350 km), which lowers the object's density to about  $1.8 \text{ g/cm}^3$ , a value closer to the densities of other large TNOs. We present unpublished and also reprocessed Herschel and Spitzer mid- and far-infrared measurements. We compare 100- and 160- $\mu\text{m}$  thermal lightcurve amplitudes - originating from Haumea itself - with models of the total measured system fluxes (ring, satellite, Haumea) from 24 – 350  $\mu\text{m}$ . The combination with results derived from the occultation measurements allows us to reinterpret the object's thermal emission. Our radiometric studies show that Haumea's crystalline water ice surface must have a thermal inertia of about  $5 \text{ J K}^{-1} \text{ m}^{-2} \text{ s}^{-1/2}$  (combined with a root mean square of the surface slopes of 0.2). We also have indications that the satellites (at least Hi'iaka) must have high geometric albedos  $\gtrsim 0.5$ , otherwise the derived thermal amplitude would be inconsistent with the total measured system fluxes at 24, 70, 100, 160, 250, and 350  $\mu\text{m}$ . The high albedos imply sizes of about 300 and 150 km for Hi'iaka and Namaka, respectively, indicating unexpectedly high densities  $> 1.0 \text{ g cm}^{-3}$  for TNOs this small, and the assumed collisional formation from Haumea's icy crust. We also estimated the thermal emission of the ring for the time period 1980-2030, showing that the contribution during the Spitzer and Herschel epochs was small, but not negligible. Due to the progressive opening of the ring plane, the ring emission will be increasing in the next decade when JWST is operational. In the MIRI 25.5  $\mu\text{m}$  band it will also be possible to obtain a very high-quality thermal lightcurve to test the derived Haumea properties.

*Keywords:*

---

## 1. Introduction

Haumea is a large trans-Neptunian object (TNO) discovered in 2003, with pre-discovery observations going back to Palomar Mountain DSS<sup>2</sup> images from 1955. Its very blue color (Tegler et al. 2007) and a surface covered with crystalline water ice (Merlin et al. 2007; Tegler et al. 2007; Trujillo et al. 2007) makes it very unique among the large TNOs. It is known to have two satellites (Brown et al. 2005, 2006) and a ring (Ortiz et al. 2017). Both satellites show signs of water ice on the surface (Barkume et al. 2006; Fraser and Brown 2009), and the water-ice absorption features are at least as deep as Haumea's. These moons are thought to have been formed either by a catastrophic impact that excavated them from the proto-Haumea ice mantle (Brown et al. 2007) or from rotational fission (Ortiz et al. 2012).

---

<sup>1</sup> $D_{\text{equ}} = 2 \cdot (a \cdot b \cdot c)^{1/3}$ .

<sup>2</sup>Digitized Sky Survey

Brown et al. (2007) reported that several other dynamically clustered objects show similar water ice absorption features and proposed that they all originated in an impact event at least 1 Gyr ago. Vilenius et al. (2018) studied a range of Haumea family members which were seen by Spitzer and Herschel. They determined Haumea-like high albedos (average 0.48) and a distinct slope of the cumulative size distribution, different from dynamical interlopers. Lacerda et al. (2008) and Lacerda (2009) performed multi-color lightcurves and found indications for surface heterogeneity on Haumea, some parts appearing to be redder and darker than the rest. However, Pinilla-Alonso et al. (2009) did not see any significant variations in their spectra taken at different rotational phases. More sensitive NIR spectroscopy measurements (Gourgeot et al. 2016) confirmed the presence of crystalline water ice over large parts of the surface and also showed that the so-called dark red spot (DRS) region was slightly redder spectrally, yet, still showing the crystalline ice signature.

Based on a large visible lightcurve amplitude, a fast rotation, and assuming hydrostatic equilibrium, Rabinowitz et al. (2006) estimated the dimensions of  $980 \text{ km} < a < 1250 \text{ km}$ ,  $540 \text{ km} < b < 759 \text{ km}$ , and  $430 \text{ km} < c < 498 \text{ km}$  (ellipsoidal axes  $a > b > c$ ) for a triaxial rotationally deformed Haumea with a homogeneous geometric albedo of  $p_V = 0.6 - 0.7$ . Stansberry et al. (2008) conducted Spitzer-MIPS  $70\text{-}\mu\text{m}$  observations and combined it with visible photometry. Their radiometric analysis resulted in a geometric albedo of  $0.84^{+0.10}_{-0.20}$  and a Spitzer-derived radiometric size of  $1150^{+250}_{-100} \text{ km}$ . They also list a size of  $1350 \pm 100 \text{ km}$  referring to Rabinowitz et al. (2005). Lellouch et al. (2010) combined the Spitzer-MIPS data with Herschel-PACS measurements at  $100$  and  $160 \mu\text{m}$ . They found an equivalent diameter ( $D_{equ}$ ) of  $\sim 1300 \text{ km}$  (radiometric diameters between  $1230$  and  $1324 \text{ km}$ ) and a geometric albedo of  $0.70\text{-}0.81$ . The  $100\text{-}\mu\text{m}$  thermal lightcurve was explained by an elongated body with an axis ratio  $a/b \approx 1.3$  and a low thermal inertia of  $0.2\text{-}0.5 \text{ J m}^{-2} \text{ s}^{-1/2} \text{ K}^{-1}$  (NEATM  $\eta < 1.15\text{-}1.35$ ; for more information on the NEATM and the beaming parameter  $\eta$  see Harris 1998). Fornasier et al. (2013) included additional Herschel measurements at  $70$ ,  $250$ , and  $350 \mu\text{m}$ . They derived a radiometric size of  $1239.5^{+68.7}_{-57.8} \text{ km}$  and a geometric albedo  $p_V$  of  $0.804^{+0.062}_{-0.095}$  based on a NEATM fit with  $\eta = 0.95^{+0.33}_{-0.26}$ .

Lockwood et al. (2014) combined system-resolved HST data with re-analyzed Spitzer-MIPS  $70\text{-}\mu\text{m}$  data. They concluded that Haumea's extreme shape is the cause of the large amplitude optical lightcurve, but also some longitudinal surface heterogeneity is needed to explain the different lightcurve minima and maxima. The axis of their best-fit Jacobi triaxial ellipsoid had lengths of  $1,920 \times 1,540 \times 990 \text{ km}$  ( $2a \times 2b \times 2c$ ) and a high density of about  $2.6 \text{ g cm}^{-3}$ . Santos-Sanz et al. (2017) presented  $100\text{-}$  and  $160\text{-}\mu\text{m}$  thermal lightcurves of Haumea obtained by the Herschel-PACS instrument apparently also showing the  $100 \mu\text{m}$  lightcurve asymmetry connected to the DRS. The radiometric studies implied a low thermal inertia ( $< 0.5 \text{ J m}^{-2} \text{ s}^{-1/2} \text{ K}^{-1}$ ) and a phase integral<sup>3</sup> larger than  $0.73$  for Haumea's surface. The best size estimate is given for a triaxial ellipsoid with  $a = 961 \text{ km}$ ,  $b = 768 \text{ km}$ ,  $c = 499 \text{ km}$ , leading to a "mean area-equivalent diameter" of  $1309 \text{ km}$ , and  $p_V = 0.71$ , in agreement with previous radiometric studies. Vilenius et al. (2018) used the occultation results together with previously published fluxes by Fornasier et al. (2013) to determine a NEATM  $\eta$  of  $1.74$ . Combining  $\eta$  with the thermal parameter  $\Theta$  via the  $\eta\text{-}\Theta$ -relation (Lellouch et al. 2013) gave a thermal inertia estimate of  $\Gamma \sim 1 \text{ J m}^{-2} \text{ s}^{-1/2} \text{ K}^{-1}$ . Satellite and ring contributions were neglected in previous aforementioned studies.

The recent occultation results (Ortiz et al. 2017) are in contradiction to the published radiometric properties (size, albedo, thermal inertia) and the hydrostatic equilibrium assumption. The occultation event combined with the optical lightcurve amplitude leads to a much larger body size with about  $2,322 \text{ km}$  for Haumea's longest axis ( $2a$ ), implying a density below  $1.9 \text{ g cm}^{-3}$  (for the derived equivalent diameter of  $1595 \text{ km}$ ) and a geometric albedo of only  $0.51$ .

In this work, we present new and updated infrared measurements and reinterpret the object's thermal infrared emission in the light of the occultation results. In section 2 we present the published thermal data set from Spitzer and Herschel-SPIRE, and also the re-analyzed data from Herschel-PACS. In section 3 we look at Haumea's spin-shape solution (Ortiz et al. 2017), derived from the multi-chord occultation, and re-interpret the corresponding thermal measurements. In section 4 we discuss our results and put them in context with other icy bodies in the Solar System. Conclusions and an outlook to future studies will be given in section 5.

---

<sup>3</sup>The phase integral  $q$  allows to calculate an object's bolometric Bond albedo  $A$ :  $A = p \cdot q$ , with  $p$  being the bolometric geometric albedo, assumed to be equal to the V-band albedo  $p_V$ .

## 2. Thermal infrared observations

### 2.1. Spitzer-MIPS observations in 2005/2007

Spitzer-MIPS (Werner et al. 2004; Rieke et al. 2004) 24/70- $\mu\text{m}$  measurements were taken on 2005 June 20/22 (listed in the Spitzer Heritage Archive under "Santa", AORKEYs 13803008, 13802752) and 2007 July 13-19 (AORKEYs 19179520, 19179776, 19180032). Stansberry et al. (2008) published an upper limit of 0.022 mJy in the 24- $\mu\text{m}$  band and 7.8 mJy (S/N of 5.3) in the 70- $\mu\text{m}$  band, derived from the two 25-min measurement in 2005. A new data reduction confirmed the 24- $\mu\text{m}$  non-detection (in 13803008) and gave a marginal (S/N $\sim$ 2) 24- $\mu\text{m}$  detection at  $0.026 \pm 0.012$  mJy (individual background-subtracted mosaics for 13802752). At 70  $\mu\text{m}$ , the new calibrated in-band fluxes are  $7.6 \pm 1.6$  mJy (from background-subtracted combined images) or  $10.9 \pm 1.8$  mJy (13802752) and  $4.3 \pm 2.1$  mJy (13803008) for the individual background-subtracted mosaics. The two measurements are separated by about 65 degrees in rotational phase, which makes the separate fluxes more useful.

In the case of the three 176-min observations in 2007, a recent reduction by Lockwood et al. (2014) combined the data in blocks of 44 min of the same rotational phases by using the  $3.915341 \pm 0.000005$  h rotation period from Lellouch et al. (2010). The new 70- $\mu\text{m}$  fluxes are listed in Table 2 in Lockwood et al. (2014), but times are given in the Haumea reference frame. We added 423.45 min light-travel time to obtain the Spitzer-centric measurement times (for compatibility with other observations, our IR database requirements, and our model setup). The observed MIPS thermal flux increase and decrease were found to be positively correlated (on a 97% level) with the HST optical lightcurve, indicating a shape-driven origin. The Lockwood et al. (2014) 70- $\mu\text{m}$  fluxes show a fitted minimum level close to 12 mJy and an amplitude of 4 mJy. However, the fit was done via a Jacobi ellipsoid ( $1920 \times 1540 \times 990$  km) and several of the MIPS points deviate considerably, with the lowest values around 8 mJy and the highest close to 20 mJy.

The color correction for Haumea-like SEDs was estimated to be 1.28 for the 24- $\mu\text{m}$  band (see also Table 4.16 in the MIPS Instrument Handbook<sup>4</sup> for blackbodies in the temperature range between 30 and 50 K). The color correction at 70  $\mu\text{m}$  is 0.89 (see also Stansberry et al. 2007, Table 2, color corrections for black bodies with temperatures in the range between 30 and 60 K). We divided the above fluxes by these factors to obtain mono-chromatic flux densities at the 23.68 and 71.42- $\mu\text{m}$  reference wavelengths. In addition, we added 6% calibration uncertainty to all MIPS flux errors when combining Spitzer with Herschel measurements for radiometric size and albedo determinations, as recommended in Lockwood et al. (2014).

In Fornasier et al. (2013) the lightcurve-averaged and color-corrected flux density at 71.42  $\mu\text{m}$  is given with  $15.83 \pm 1.20$  mJy, in good agreement with the averaged Lockwood et al. (2014) fluxes when taking the color-correction factor of 0.89 into account.

### 2.2. Herschel-PACS/SPIRE observations of Haumea

The Herschel Space Observatory (Pilbratt et al. 2010) also performed a range of measurements on Haumea with the PACS (Poglitsch et al. 2010) and SPIRE (Griffin et al. 2010) instruments in the framework of the large key project "TNOs-are-Cool!" (Müller et al. 2009). Subset of these data were presented in Lellouch et al. (2010), Fornasier et al. (2013), and Santos-Sanz et al. (2017).

*Herschel-SPIRE.* For our analysis we took the SPIRE measurements from 2011 January 7/9 as presented by Fornasier et al. (2013). The two 35-min observation blocks were combined to eliminate the strong background structures. The measurements are separated by 49.94 hour which corresponds to almost exactly 270 degrees in rotational phase, but both epochs are close to the mid-flux in the optical lightcurve and can therefore be combined.

*Herschel-PACS.* The Herschel-PACS observation were taken on 2009 December 23/25 (OBSIDs 1342188470, 1342188520; 100/160  $\mu\text{m}$ ), and 2010 June 20/21 (1342198851, 1342198903/904/905/906; 70/100/160  $\mu\text{m}$ ). Lellouch et al. (2010) presented an analysis of the 2009 lightcurve data, and Fornasier et al. (2013) of the 2010 data. Santos-Sanz et al. (2017) focused on the two lightcurve data sets from 2009 and 2010.

In the present paper, we re-analyzed and re-calibrated all PACS observations with the latest tools and techniques (Kiss et al. 2014). The reprocessing includes a better noise characterization, the elimination of the background which

---

<sup>4</sup><http://irsa.ipac.caltech.edu/data/SPITZER/docs/mips/mipsinstrumenthandbook/>

Table 1: Epochs and observing geometry for all thermal measurements. PACS and SPIRE are Herschel instruments, the observations are labeled with the Observation ID (OBSID), and the photometric bands are at 70, 100, 160, 250, 350, and 500  $\mu\text{m}$ . MIPS is a Spitzer instrument, the observations are connected to an AORKEY, the relevant bands are at 24 and 70  $\mu\text{m}$ . The Haumea heliocentric distance ( $r_{\text{helio}}$ ), the observatory-Haumea distance ( $\Delta$ ), and the phase angle  $\alpha$  are given for the observation mid-time. The one-way light-travel times vary between 421.97 and 426.33 minutes. Note, that for the flux determination it was necessary to combine different measurements (see text), the corresponding observing epochs in Tables A.6, A.7, and A.8 are therefore different. Observations were taken from the Spitzer Heritage Archive (SHA) and the Herschel Science Archive (HSA). The PACS data are based on 10 individual 3.5(or 3.0) arcmin satellite scans, separated by 10 arcsec and either in 70 or 110° scan angles with respect to the instrument reference frame. the lightcurve background measurement. The 1-3 days separation of the measurements allows to reconstruct mutual backgrounds while Haumea is always in the center of the map.

Instrument	Identifier	Band(s)	Start time UT	Duration [sec]	mid-time JD (+2450000.0)	$r_{\text{helio}}$ [AU]	$\Delta$ [AU]	$\alpha$ [°]	Comments
MIPS	13803008	24/70	2005-Jun-20 17:20:37	1477	3542.23125	51.242	50.906	1.07	''Santa'' in SHA
MIPS	13802752	24/70	2005-Jun-22 09:11:29	1477	3543.89167	51.242	50.929	1.08	''Santa'' in SHA
MIPS	19179520	24/70	2007-Jul-13 11:01:22	10294	4295.01886	51.152	50.885	1.10	''2003 EL61'' in
MIPS	19179776	24/70	2007-Jul-16 04:23:05	10297	4297.74229	51.152	50.924	1.11	''2003 EL61'' in
MIPS	19180032	24/70	2007-Jul-19 06:43:33	10296	4300.83983	51.152	50.969	1.12	''2003 EL61'' in
PACS	1342188470	100/160	2009-Dec-23 05:52:01	12084	5188.81439	51.028	51.262	1.08	lightcurve 1
PACS	1342188520	100/160	2009-Dec-25 06:13:39	2420	5190.77348	51.028	51.232	1.09	background
PACS	1342198851	100/160	2010-Jun-20 20:45:11	15514	5368.45449	51.001	50.737	1.12	lightcurve 2
PACS	1342198903	70/160	2010-Jun-21 22:42:00	568	5369.44912	51.001	50.752	1.12	scan map
PACS	1342198904	70/160	2010-Jun-21 22:52:31	568	5369.45642	51.001	50.752	1.12	cross-scan map
PACS	1342198905	100/160	2010-Jun-21 23:03:02	568	5369.46373	51.001	50.752	1.12	scan map
PACS	1342198906	100/160	2010-Jun-21 23:13:33	568	5369.47103	51.001	50.752	1.12	cross-scan map
SPIRE	1342212360	250/350/500	2011-Jan-07 07:08:50	2111	5568.81002	50.971	50.994	1.12	small scan map
SPIRE	1342212414	250/350/500	2011-Jan-09 09:05:18	2111	5570.89090	50.971	50.962	1.12	follow-on map

is very critical for faint sources in the two long-wavelength channels at 100 and 160  $\mu\text{m}$ , an object-centered stacking of multiple measurements, and a better understanding of the flux calibration for faint sources (see also Klaas et al. 2018; Balog et al. 2014). The flux errors were determined by performing aperture photometry at random places in the close vicinity of Haumea and then combining with the PACS photometer intrinsic absolute flux calibration error of 5% (Balog et al. 2014). The final Haumea maps - together with all ''TNOs-are-Cool'' observations (more than 400 h of Herschel observing time; Müller et al. 2009) - were uploaded to the HSA<sup>5</sup> as ''User Provided Data Products (UPDP<sup>6</sup>)''. The details of the procedure and the new products are given in two specific release notes: ''User Provided Data Products of Herschel/PACS photometric light curve measurements of trans-Neptunian objects and Centaurs<sup>7</sup>'' and ''User Provided Data Products from the TNOs are Cool! A Survey of the trans-Neptunian Region Herschel Open Time Key Program<sup>8</sup>''.

Two sets of 100/160- $\mu\text{m}$  lightcurves were taken: (1) A 3h21min sequence on 2009 December 23, followed by a ~40 min background measurement on 2009 Dec 25. However, Haumea had moved by more than 80 arcsec between both measurements (Haumea's apparent motion was about 1.7 arcsec/hour) which means that the relevant background region had moved to the edge of the 105×210 arcsec FOV of the PACS bolometer array in the follow-up measurements on Dec 25. Haumea's sky background in the long-duration measurement is therefore only poorly characterized and part of the observed flux variations are very likely related to the structured background along Haumea's path. (2) A 4h18min sequence on 2010 June 20. In this second sequence, Haumea moved about 5.6 arcsec on the sky during the 4.3 hours (compared to the ~7/12 arcsec FWHM of a point-source PSF at 100/160  $\mu\text{m}$ , respectively). The sky background in these two bands were taken from the measurements taken on the following day, when Haumea had moved about 30 arcsec. We performed aperture photometry on the background-subtracted images, and color-corrected the resulting fluxes (see also Santos-Sanz et al. 2017). For the 100 and 160  $\mu\text{m}$  lightcurve data we merged 3 and 6

<sup>5</sup>Herschel Science Archive

<sup>6</sup><https://www.cosmos.esa.int/web/herschel/user-provided-data-products>

<sup>7</sup>[http://www.mpe.mpg.de/~tmueller/sbnaf/doc/tnosarecool\\_hsa\\_upload\\_v1.pdf](http://www.mpe.mpg.de/~tmueller/sbnaf/doc/tnosarecool_hsa_upload_v1.pdf)

<sup>8</sup>[http://www.mpe.mpg.de/~tmueller/sbnaf/doc/tno\\_lightcurve\\_hsa\\_upload\\_v1.pdf](http://www.mpe.mpg.de/~tmueller/sbnaf/doc/tno_lightcurve_hsa_upload_v1.pdf)

repetitions, respectively. For the overlap, the shift between the 100  $\mu\text{m}$  data points is 1 repetition, but it is 3 repetitions between the 160  $\mu\text{m}$  data points, leading to an oversampled of a factor of 3(6) at 100(160)  $\mu\text{m}$ . The final numbers are given in Tables A.6, A.7, and A.8.

With the knowledge of Haumea’s precise rotation period, it is possible to combine the 100/160- $\mu\text{m}$  lightcurves from December 2009 and June 2010 to plot the obtained fluxes as a function of rotational phase using  $P_{rot} = 3.915341$  h (Santos-Sanz et al. 2017; Thirouin 2013), and a (Herschel-centric) reference date of JD = 2455188.743985 (phase  $\phi=0$ ), the start time of the observations. It is worth to note that the light travel times and the rotational phase shifts between the two lightcurve epochs are only 13.5 s and 0.0009, respectively, much shorter than typical measurement time of a few minutes. Figure 1 shows the phase-folded 100- and 160- $\mu\text{m}$  data, respectively.

The 100- $\mu\text{m}$  double-peaked sinusoidal fit gave  $A_0 = 25.23 \pm 0.89$  mJy and  $A_1 = 3.12 \pm 1.25$  mJy (Flux =  $A_0 + A_1 \sin(\phi)$ ). Overall, the consideration of the 1<sup>st</sup> lightcurve from December 2009 seems to increase the lightcurve amplitude a bit, but it gives almost exactly the same mean ( $A_0$ ). In the caption of Fig. 1 we explain the data and model fits. We see a definite lightcurve at 100  $\mu\text{m}$ , and it is likely asymmetric (lower peak at  $\phi=0.6$ ). There are some data points from the 1<sup>st</sup> lightcurve data (dark blue) that seemingly increase the amplitude, but these points are affected by single repetitions that provide a very high flux density. They all happen in the 1<sup>st</sup> lightcurve with the problematic background.

The combined light curve at 160  $\mu\text{m}$  shows the first-epoch data in red and the second-epoch data in orange. The error bars are much larger at the 1<sup>st</sup> epoch due to the background characterization problems. We determined  $A_0=26.57 \pm 2.73$  mJy and  $A_1=4.10 \pm 3.85$  mJy. The uncertainty on  $A_1$  is very large, but produced by our  $\chi^2$  analysis of the data. We also tried to refit the 160  $\mu\text{m}$  data with a fixed lightcurve phase, as obtained from the 100  $\mu\text{m}$  lightcurve. In this case, the mean is the same, and the lightcurve amplitude is  $<2.5$  mJy, with a nearly flat (uniform) distribution between 0 and 2.5 mJy (formally the highest probability is at  $\approx 1.63$  mJy). It is worth to note that both, our 100  $\mu\text{m}$  and 160  $\mu\text{m}$  lightcurve amplitudes, correspond to  $\sim 0.3$  mag, very close to the visible lightcurve amplitude.

The four short 10-min PACS measurements from 2010 June 21 (see Table 1) are reduced in a standard way by combining the scan- and cross-scan images. The 100- and 160- $\mu\text{m}$  background maps (from 2010 June 20) were subtracted. The 70- $\mu\text{m}$  map has no dedicated background counterpart, but background confusion is less severe at these shorter wavelengths. The extracted fluxes are aperture and color corrected and come with a proper noise determination. The fluxes are given in the tables in the appendix (Tables A.6, A.7, A.8, A.9). These 3-band data can also be phased into our lightcurve data: The corresponding rotation phase is around 0.75, which is very close to the mid-flux level.

Overall, the new reduction procedure increased the reliability of the extracted fluxes and reduced the previously published peak-to-peak lightcurve amplitudes significantly. The poorly characterized background structures in the 2009 lightcurve data were the main cause for the large flux variation shown in Lellouch et al. (2010) (peak-to-peak lightcurve amplitude of  $\sim 17$  mJy at 100  $\mu\text{m}$ ) and Santos-Sanz et al. (2017) (about 10(8) mJy variation at 100(160)  $\mu\text{m}$ ).

### 3. Thermophysical model calculations

The radiometric technique (see e.g. Delbo et al. 2015 and references therein) usually takes measured thermal infrared fluxes to derive size, albedo, and thermal properties for a given object. In the case of Haumea, we follow a different approach, mainly because of the direct size measurement from the occultation event, and the unknowns in the satellite-ring contributions to the thermal signals.

#### 3.1. Using the occultation cross-section

We use the occultation-derived 2-D ellipse fit for Haumea, as measured on 2017 January 21 at around 03:09 UT ( $\pm$  about 1.5 min). Haumea’s projected shape was fit by an ellipse with  $a=852 \pm 2$  km and  $b=569 \pm 13$  km or a circle-equivalent diameter of  $2 \sqrt{852 \times 569} = 1392.5$  km ( $\pm 10.2$  km) (Ortiz et al. 2017). The lightcurves taken close in time to the occultation event showed that Haumea was very close to its minimum brightness, both in reflected light and thermal emission (see Lockwood et al. 2014; Santos-Sanz et al. 2017). Regarding the DRS, this is centered in one of the lightcurve maxima (Lacerda et al. 2008), which means that at lightcurve minimum the DRS would be in grazing view from the Earth with a tiny effect on the thermal flux.

In a first step, we use only the occultation cross section and the object’s rotational properties (Lellouch et al. 2010; Ortiz et al. 2017) to make thermophysical predictions at the Spitzer and Herschel observing epochs and geometries. The following (relevant) parameters were used in our thermophysical model (TPM) setup:

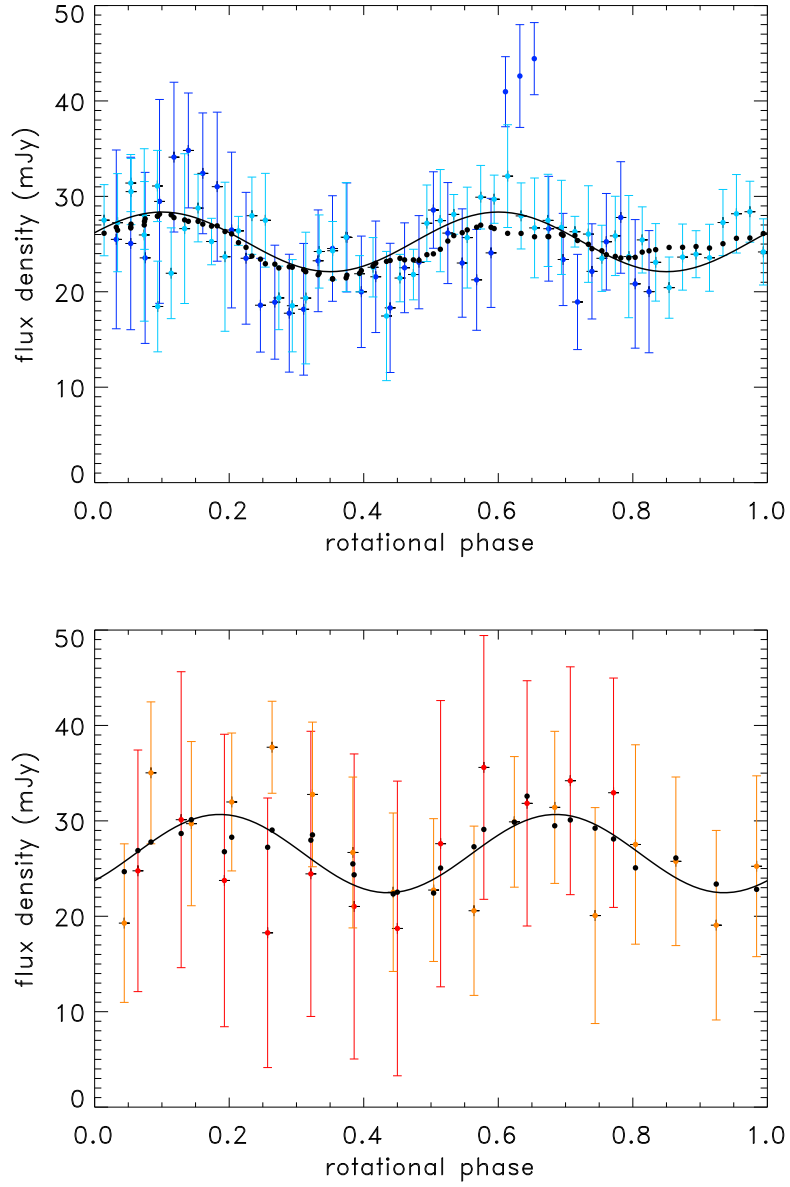


Figure 1: The two sets of 100- (top) and 160- $\mu\text{m}$  (bottom) Herschel-PACS lightcurve measurements combined (see text for details). The zero phase corresponds to  $\text{JD} = 2455188.743985$ . The dark blue(red) points are of the 1<sup>st</sup> epoch, and the light blue(orange) ones are of the 2<sup>nd</sup> epoch. The solid black curve is the sinusoidal fit. The curve drawn by the black dots is a smooth curve from the original data (the fit is made with the original data, not the smoothed one, without the three outliers around  $\phi=0.65$ ). The 100  $\mu\text{m}$  lightcurve seems to be asymmetric with the lower peak at  $\phi=0.6$ .

- For the interpretation of the fitted occultation ellipse we use an oblate spheroid with  $a = b = 852$  km;  $c = 513$  km which resembles the occultation ellipse when projecting the oblate spheroid under an aspect angle of  $76.2^\circ$ .
- We use the occultation-derived rotation poles at (RA, Dec)=( $285.1^\circ$ ,  $-10.6^\circ$ ) and (RA, Dec)=( $312.3^\circ$ ,  $-18.6^\circ$ ), named pole 1 and pole 2, respectively (in ecliptic coordinates: ( $285.2^\circ$ ,  $+12.1^\circ$ ) and ( $309.6^\circ$ ,  $-0.8^\circ$ )); however, pole 1 was given priority in Ortiz et al. (2017) because of the long-term lightcurve amplitude behavior of Haumea and the agreement with Hi'iaka's orbital pole position.
- The object's rotation period was found to be  $P_{rot} = 3.915341$  hours (Santos-Sanz et al. 2017).
- The rotationally averaged absolute magnitude of the Haumea-system is  $H_V = +0.35 \pm 0.06$ , but we use the  $H_V$  value of Haumea's main body at the time of the occultation:  $0.35 + 0.14 + 0.32/2$  mag (to account for the satellites and the lightcurve amplitude; Ortiz et al. 2017) =  $0.65$  mag.
- Then, the object's geometric albedo can be calculated (Harris 1998):

$$p_V = (1329/D(\text{km}))^2 \cdot 10^{(-0.4H)} \quad (1)$$

The resulting geometric albedo connected to the occultation ellipse size is then  $0.51 \pm 0.02$  (Ortiz et al. 2017) or  $\pm 0.05$  if we take the 10.2-km size error and a conservative  $\pm 0.1$  mag error for  $H_{mag}$  into account.

- For the phase integral we applied the formula by Brucker et al. (2009):  $q = 0.336p_V + 0.479$ . This led to  $q = 0.65$  (for  $p_V = 0.51$ ). Whenever relevant, we tested also a wider range of  $q = 0.45$  to  $0.85$  to account for the unknown scattering properties on Haumea's surface.
- Like in most radiometric studies, we use a bolometric emissivity  $\epsilon = 0.9$  in the MIPS/PACS range, and a lower emissivity of  $0.8$  at sub-millimeter wavelengths in the SPIRE range (see Müller 2002, Fornasier et al. 2013; Lellouch et al. 2016; Lellouch et al. 2017).
- We consider a very wide range of surface roughness values (as a free parameter) ranging between  $0.1$  (very smooth) and  $0.9$  (extremely rough) in r.m.s. of surface slopes. However, the lower range with r.m.s  $< 0.5$  seems to be more realistic for TNOs (see findings in Fornasier et al. (2013)).
- The thermal inertia is our free parameter and we test a range between  $0.01 \text{ J K}^{-1} \text{ m}^{-2} \text{ s}^{-1/2}$  (extremely low thermal conductivity) and  $100 \text{ J K}^{-1} \text{ m}^{-2} \text{ s}^{-1/2}$  (extremely high conductivity considering the low-temperature environment at 50 AU).
- The differences in Spitzer-Haumea and Herschel-Haumea distances and phase angles are small and lead to negligible differences in the TPM fluxes of only 1-2% (assuming low thermal inertia below  $5 \text{ J K}^{-1} \text{ m}^{-2} \text{ s}^{-1/2}$ ) or less for thermal inertias  $> 5 \text{ J K}^{-1} \text{ m}^{-2} \text{ s}^{-1/2}$ , for the 6-yr span of thermal observations (Tbl. reftbl:obs).

Using the above settings, we can make flux predictions for the full range of thermal inertias and roughness levels for the specific occultation size. The calculations are done via a TPM (Lagerros 1996, 1997, 1998; Müller and Lagerros 1998; Müller 2002) and, in the first step, by using a spheroid resembling the fitted occultation ellipse (see explanation above). The TPM predictions are shown in Fig. 2. The illuminated side of a TNO coincides with the visible hemisphere given the typical small phase angle of the observations. However, the thermal fluxes (default values are shown as diamonds) decrease with increasing thermal inertias (more heat is transported to the night side). At  $\sim 10 \text{ J K}^{-1} \text{ m}^{-2} \text{ s}^{-1/2}$  Haumea is almost isothermal (except at the poorly illuminated polar regions) with the 30-40 K zone reaching latitudes of above  $60^\circ$ . At much larger thermal inertias more and more heat goes to the subsurface (lowering the effective temperature) and the warm terrain shrinks towards the equatorial zone (still isothermal at each latitude) which explains the steep decrease at very high thermal inertias. The assumptions of a high/low surface roughness (dashed line below and dashed-dotted line above the diamonds) produces higher/lower fluxes, but the influence of roughness shrinks with increasing thermal inertia. We also tested the influence of the phase integral  $q$  ( $0.45 < q < 0.85$ ), but the lines are within the low/high roughness corridor, with the  $q=0.45$  prediction close to the "high roughness" levels, and the  $q=0.85$  predictions close to the "low roughness" dashed line (see Fig. 2, bottom).

These predictions can now be compared with the calibrated, color-corrected absolute flux densities. We take the fluxes at thermal lightcurve minimum since the occultation happened close to the minimum (Santos-Sanz et al. 2017):  $\approx 12$  mJy at  $70\ \mu\text{m}$  (estimated from Figure 1 in Lockwood et al. (2014)),  $22 \pm 1.5$  mJy at  $100\ \mu\text{m}$ , (horizontal dashed and dotted lines on the left side in Figure 2 top and bottom part), and  $22.5 \pm 3$  mJy at  $160\ \mu\text{m}$  (see fit parameters  $A_0$  and  $A_1$  above). But there is one problem with that comparison: the thermal measurements include contributions from the ring and Haumea’s satellites (see discussion in Section 3.3). The Haumea-only fluxes (subtracting the smallest possible ring-satellite contribution) are also shown in the figure as thicker solid lines on the right side of Figure 2. The intersections with the flux curves indicate the most probable thermal inertia for Haumea itself. These simple calculations are based on the measured occultation ellipse and Haumea’s H-magnitude and rotational properties, but they show that the occultation result is only compatible with the thermal measurements when the thermal inertia is larger than  $\approx 2\ \text{J K}^{-1}\ \text{m}^{-2}\ \text{s}^{-1/2}$ . This lower limit for the thermal inertia is confirmed by similar exercises at 70, 160, and  $250\ \mu\text{m}$  where we also have multiple observations. The figure shows that higher ring/satellite contributions (e.g., when assuming a less-extreme lower albedo for the satellites) would automatically lead to even higher thermal inertias for Haumea. Also the TPM assumptions for the surface roughness play a role: for a low-roughness (smooth) surface we estimate a thermal inertia of 2 (or higher), while a very rough surface would give also higher thermal inertias well above  $10\ \text{J K}^{-1}\ \text{m}^{-2}\ \text{s}^{-1/2}$ . TPM analysis of other targets (Fornasier et al. 2013; Kiss et al. 2018) indicated that lower roughness values (r.m.s. of surface slopes between 0.1 to 0.3) seem to fit better the thermal signals of dwarf planets. Looking at the influence of the phase integral shows an opposite trend: high q-values are more compatible with low thermal inertias (above  $\sim 5\ \text{J K}^{-1}\ \text{m}^{-2}\ \text{s}^{-1/2}$ ), while q-values below 0.5 would require Haumea to have  $\Gamma$  well above  $10\ \text{J K}^{-1}\ \text{m}^{-2}\ \text{s}^{-1/2}$  (Figure 2 bottom part).

### 3.2. Using the occultation-lightcurve derived 3-D size-spin-shape solution

The above exercise (Fig. 2) used minimum fluxes in each band for a direct comparison with the occultation 2-D results. But the five thermal lightcurves (single MIPS  $70\ \mu\text{m}$ ; two-epoch PACS  $100/160\ \mu\text{m}$  lightcurves) contain additional information. The absolute fluxes are “contaminated” by the unknown ring/satellite contributions, but the lightcurve amplitude is directly connected to Haumea itself (Lockwood et al. 2014). For the interpretation of the thermal lightcurves we use the Ortiz et al. (2017) 3-axes ellipsoid with a default size of  $a = (1161 \pm 30)$  km,  $b = (852 \pm 2)$  km, and  $c = (513 \pm 16)$  km ( $a/b = 1.36$  and  $b/c = 1.66$ ) and a volume-equivalent diameter of  $2 \cdot (1161 \cdot 852 \cdot 513)^{1/3} = 1595$  km. In addition, we also consider the more extreme solution (based on a maximum of 5% for the visual brightness contribution of the ring to the observed magnitudes) with  $2a = 2520$  km ( $a/b = 1.48$ ;  $D_{\text{equ}} = 1632$  km), also given in Ortiz et al. (2017). The corresponding thermal lightcurve amplitude decreases with increasing thermal inertia (see Figure 3), with only very little influence by the surface roughness assumptions or the value for the phase integral (not shown in the figure). The “default” occultation model is shown with a solid line, the extreme case with  $2a = 2520$  km produces a larger amplitude (shown as dashed line). The  $100\ \mu\text{m}$  lightcurve amplitude which was fitted to the observed fluxes (see Figure 1) is over-plotted (solid horizontal line). The formal amplitude error from the fit is also shown (dashed horizontal lines). The  $100\ \mu\text{m}$  lightcurve amplitude indicates that Haumea must have a thermal inertia in an estimated range between  $\sim 2$  and about  $10\ \text{J m}^{-2}\ \text{s}^{-1/2}\ \text{K}^{-1}$ . If the a-axis is more extended (dashed line in Fig. 3) then the limits are between 4 and about  $15\ \text{J m}^{-2}\ \text{s}^{-1/2}\ \text{K}^{-1}$ . The lightcurves at  $70\ \mu\text{m}$  (MIPS) and  $160\ \mu\text{m}$  give a very similar picture, although the formal errors are bigger. Figure 3 explains nicely why previous studies (Lellouch et al. 2010; Santos-Sanz et al. 2017) resulted in much smaller thermal inertias for Haumea. In these projects, the light curve amplitudes were heavily overestimated due to the poorly characterised background. In addition, previous assumed shape models (based on hydrostatic equilibrium) were less elongated than the one from the occultation, and the derived radiometric size was smaller. Both aspects pushed the derived thermal inertia to very small values. Having the occultation-derived shape, spin pole and size, also allowed us to look into the shift between the optical and thermal lightcurves. We calculated this shift for thermal inertias ranging from  $\Gamma = 0\ \text{J m}^{-2}\ \text{s}^{-1/2}\ \text{K}^{-1}$  (in phase with the optical lightcurve) to  $\Gamma = 25\ \text{J m}^{-2}\ \text{s}^{-1/2}\ \text{K}^{-1}$  (thermal lightcurve is delayed with respect to the optical). We determined delay times (see also Santos-Sanz et al. 2017) of up to 5 min (or  $\sim 0.02$  in rotational phase) for the current aspect angle, but our observations are clearly not accurate enough to measure this effect directly. However, the optical-thermal delay might still be an interesting approach for other targets (with less-extreme shapes) to constrain the object’s thermal inertia.



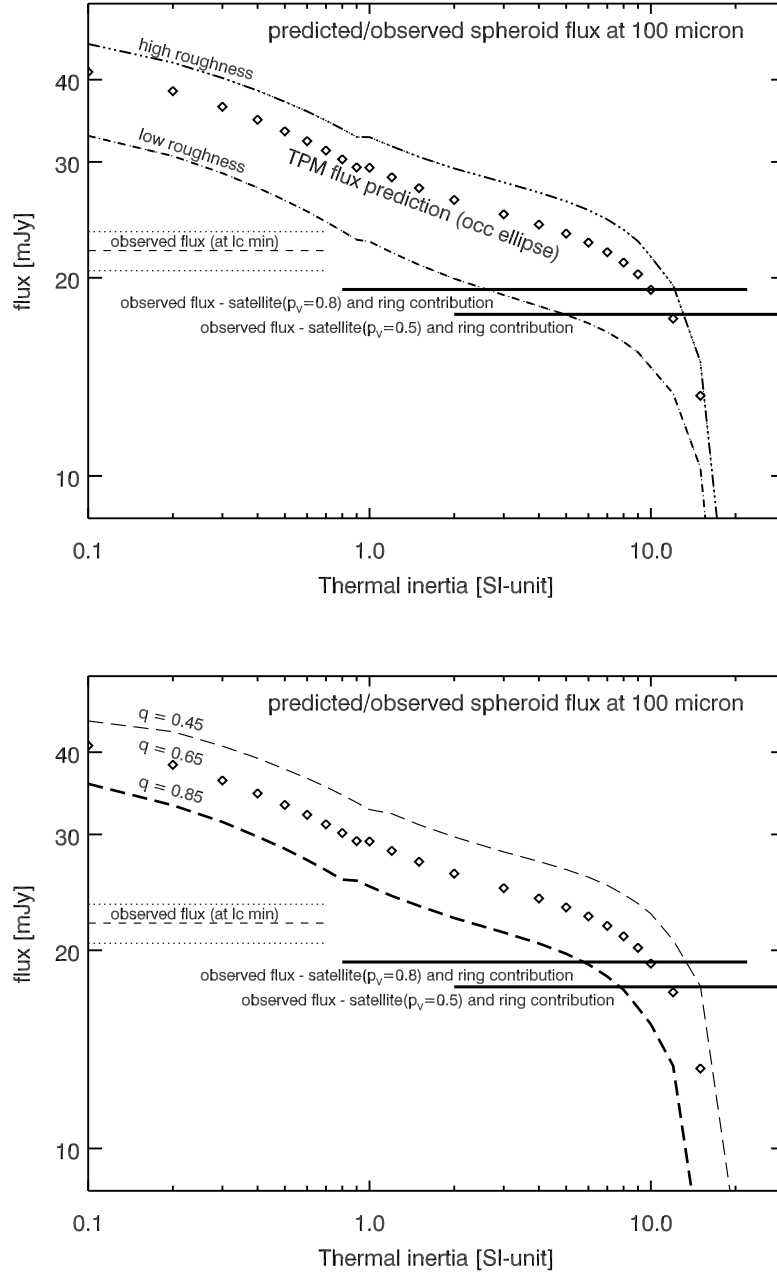


Figure 2: TPM 100- $\mu\text{m}$  flux calculations using only the occultation 2-D ellipse information. The measured 100- $\mu\text{m}$  flux (of the thermal lightcurve minimum) is over-plotted: Left side within the figure: the observed Haumea-ring-satellite fluxes (with errors shown as dotted lines); right side: the estimated satellite-ring contribution was subtracted from the observed flux, assuming an albedo of  $p_V=0.8$  for the satellites (horizontal top solid/dashed lines), and  $p_V=0.5$  (lower solid line). Top: Using a wide range of extreme roughness levels on the surface. Bottom: Using a wide range of phase integrals (from 0.45 to 0.85). The intersections between model and observed fluxes indicate that Haumea's thermal inertia must be above  $\sim 2$  and below  $\sim 20 \text{ J m}^{-2} \text{ s}^{-1/2} \text{ K}^{-1}$

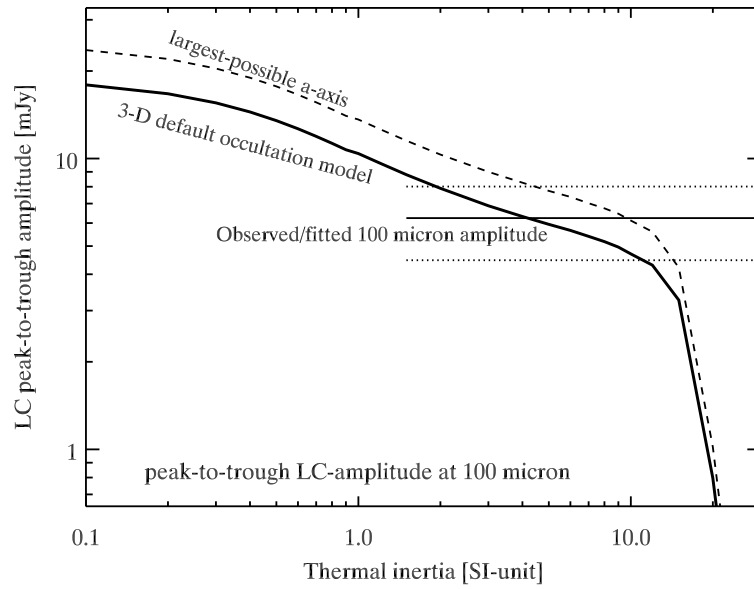


Figure 3: TPM 100- $\mu\text{m}$  lightcurve amplitudes for the default 3-D spin-shape-size solution derived from the occultation (solid line) and using the largest possible a-axis extension (see Ortiz et al. 2017) (dashed line). The observed lightcurve amplitude is over-plotted (see Fig. 1). This approach leads to a thermal inertia above  $\sim 2$  and below  $\sim 15 \text{ J m}^{-2} \text{ s}^{-1/2} \text{ K}^{-1}$  for Haumea.

### 3.3. Estimating the thermal contribution of the satellites and the ring

Haumea is known to have two satellites (Brown et al. 2005, 2006) and a ring (Ortiz et al. 2017). Ragozzine and Brown (2009) determined the mass of Haumea’s satellites from the orbits in the framework of a three point mass model ( $1.79 \pm 0.11 \cdot 10^{19}$  kg for Hi’iaka, and  $1.79 \pm 1.48 \cdot 10^{18}$  kg for Namaka). Using a realistic density estimate of  $\rho = 0.5\text{--}1.5$  g/cm<sup>3</sup> for both moons, the size ranges are  $D_H = 350 \pm 50$  km, and  $D_N = 150 \pm 50$  km for Hi’iaka and Namaka, respectively. Additionally, Brown et al. (2006) listed the moons’ brightnesses to be  $5.9 \pm 1.5\%$  and  $1.5 \pm 0.5\%$  of Haumea’s brightness, while Ragozzine and Brown (2009) reported Hi’iaka to be  $\approx 10$  times fainter than Haumea and Namaka  $\approx 3.7$  times fainter than Hi’iaka, corresponding to  $\sim 3.5$  and  $5.1$  mag for their absolute magnitudes<sup>9</sup>, given Haumea’s absolute magnitude,  $H_V = 0.49$  mag (Ortiz et al. 2017). We predicted the flux densities of Haumea’s satellites using a NEATM model (Harris 1998) for the above range of possible mass-related sizes and albedos (fulfilling the H-magnitude constraint), and assuming the Brucker et al. (2009) phase-integral-albedo relation. We consider the usage of the NEATM as appropriate in case of the satellites where no spin properties (rotation period and/or spin-axis orientation) are known. In Table 2 we list the corresponding flux predictions assuming a beaming parameter of  $\eta = 1$ . This  $\eta$ -value is close to the weighted mean value of 1.07 derived from combined Herschel and Spitzer observations of 85 TNOs and Centaurs (Lellouch et al. 2013).

Table 2: NEATM predictions for Haumea’s satellites, assuming a beaming parameter  $\eta=1.0$ , and a constant emissivity of  $\epsilon=0.9$ . "PhaseInt": value for the phase integral.

Diameter (km)	Albedo $p_V$	PhaseInt q	Hi’iaka flux (mJy) at					
			24 $\mu$ m	70 $\mu$ m	100 $\mu$ m	160 $\mu$ m	250 $\mu$ m	350 $\mu$ m
300	0.79	0.74	0.002	0.86	1.33	1.31	0.89	0.58
350	0.58	0.67	0.011	1.85	2.52	2.24	1.44	0.91
400	0.44	0.63	0.023	2.93	3.78	3.22	2.03	1.27
Diameter (km)	Albedo $p_V$	PInteg. q	Namaka flux (mJy) at					
			24 $\mu$ m	70 $\mu$ m	100 $\mu$ m	160 $\mu$ m	250 $\mu$ m	350 $\mu$ m
140	0.83	0.76	<0.001	0.17	0.26	0.27	0.18	0.12
160	0.64	0.69	0.002	0.35	0.49	0.44	0.29	0.18
180	0.50	0.65	0.004	0.55	0.72	0.63	0.40	0.25
200	0.41	0.62	0.006	0.76	0.97	0.82	0.51	0.32

For both satellites, smaller sizes than the above stated limits would require unrealistically high geometric albedos,  $p_V > 1$ , which is not expected for inactive bodies. The two satellites give a minimum thermal emission contribution of  $\sim 1.0$  mJy at 70  $\mu$ m, 1.6 mJy at 100  $\mu$ m, 1.6 mJy at 160  $\mu$ m, 1.1 mJy at 250  $\mu$ m, and 0.7 mJy at 350  $\mu$ m (assuming  $p_V \sim 0.8$  for both). For a lower albedo of  $p_V \sim 0.5$ , the contributions at 70, 100, 160, 250, and 350  $\mu$ m are already 2.4, 3.2, 2.9, 1.8, and 1.2 mJy, respectively. We also investigated the influence of a higher beaming parameter with  $\eta=1.3$ . In this case, the satellites contribute about 20% less flux in the PACS and about 10% less in the SPIRE range.

It is worth to note here that Haumea might have more so-far undiscovered satellites, including potential shepherd satellites for the ring. They might also add a small contribution to the observed fluxes of the Haumea-ring-satellite system.

To estimate the thermal contribution of Haumea’s ring, we used the simple thermal model from Lellouch et al. (2017), itself based on a simplified version of a model for Saturn’s rings. In this model, the only source of energy for ring particles is absorbed solar radiation, but mutual shadowing - as seen both from the Sun and the observer - and optical depth effects are taken into consideration. The model further assumes that ring particles have a bolometric and spectral emissivity of unity. By analogy with Saturn’s rings, the latter assumption is certainly valid up to  $\sim 200$   $\mu$ m, but the spectral emissivity could decrease at longer wavelengths if ring particles are made of water ice. Model free parameters are the ring radius  $r$ , width  $w$ , opacity  $\tau$ , and Bond albedo  $A_b$ , related to the I/F reflectivity<sup>10</sup> and the phase

<sup>9</sup>see also <http://www.johnstonsarchive.net/astro/astmoons/am-136108.html>, retrieved on Oct 24, 2018.

<sup>10</sup>I is the intensity of light reflected by the surface and  $\pi F$  is the incident solar flux density.

Table 3: Thermal emission predictions for Haumea’s ring assuming I/F = 0.09. The first part shows the estimates (in mJy) for our Spitzer and Herschel measurements, the second part includes calculations (in  $\mu$ Jy!) for JWST-MIRI filters. During the 2005/2007 Spitzer observing epochs the ring contribution in the 24- $\mu$ m band is expected to be below 1  $\mu$ Jy and therefore negligible. The MIRI imager sensitivities (SNR = 10 in 10,000 sec) are increasing from about 1  $\mu$ Jy at 15  $\mu$ m to about 10  $\mu$ Jy at 25.5  $\mu$ m.

Observation epoch	70 $\mu$ m [mJy]	100 $\mu$ m [mJy]	160 $\mu$ m [mJy]	250/350 $\mu$ m [mJy]
Jun 2005	<0.05	-	-	-/-
Jul 2007	0.15	-	-	-/-
Dec 2009	0.4	1.0	1.2	-/-
Jun 2010	0.6	1.4	1.4	-/-
Jan 2011	-	-	-	1.4/1.0
JWST-MIRI prediction	15 $\mu$ m [ $\mu$ Jy]	18 $\mu$ m [ $\mu$ Jy]	21 $\mu$ m [ $\mu$ Jy]	25.5 $\mu$ m [ $\mu$ Jy]
early 2022	0.012	0.28	2.5	23
mid 2025	0.023	0.48	4.0	35

integral, assumed here to be equal to 0.5. We use the nominal values from (Ortiz et al. 2017), i.e.  $r = 2287$  km,  $w = 70$  km,  $\tau = 0.5$  and I/F = 0.09 (see also the discussion in Braga-Ribas et al. 2014). Although the latter quantity is the least well constrained, it has a minor effect on the ring thermal emission. We calculated the ring thermal flux for all viewing geometries from 1980 to 2030 (see Figure 4). The calculated thermal fluxes at some selected wavelengths and dates are listed in Table 3.

In the work by Santos-Sanz et al. (2017), the possible thermal contributions of the satellites Hi’iaka and Namaka were estimated to be  $\sim 6\%$  and  $1.5\%$ , respectively, but they did not consider these contributions in their radiometric analysis. And, the ring was not known at that time. Here, we subtract the summed up minimum ring-satellite contribution from the total observed Spitzer and Herschel fluxes: 0.002 mJy and 1.1 (1.2) mJy for the MIPS 24- and 70- $\mu$ m observations in 2005 (2007); 1.6 mJy, 2.6 (3.0) mJy, and 2.8 (3.0) mJy for the PACS 70, 100, and 160- $\mu$ m observations in 2009 (2010); and, 2.5 mJy and 1.7 mJy for the SPIRE 250 and 350  $\mu$ m observations in 2011. Depending on wavelengths and epoch, the Haumea-only fluxes are about 5-23% lower than the total observed fluxes for the most conservative case (with the satellites having an albedo above 0.7). In case of darker surfaces (albedo of 0.5 for the satellites), the satellite/ring contributions would increase significantly and could easily reach 1/3 of the observed total flux. However, in these cases, the Haumea model would require a very high thermal inertia well above 10 to lower its flux contribution accordingly. At the same time, the amplitude of the thermal lightcurve would also decrease, well below the observed 100 and 160  $\mu$ m amplitudes (see Figs. 3 and 5, bottom).

#### 4. Discussion

The size and shape estimate for Haumea and the ring discovery from the multi-chord occultation observation were crucial for the reinterpretation of the thermal emission measurements. From our calculations (Figs. 2 and 3), it is very likely that the satellites and the ring contributions to the measured signals are small. As a consequence, the satellites (at least Hi’iaka) must have a high albedo (very likely above 0.5), otherwise their thermal contribution would reach several milli-Jansky which is problematic when trying to match the Haumea occultation size to the ring-satellite-subtracted thermal flux. Haumea’s thermal inertia would be above  $10 \text{ J m}^{-2} \text{ s}^{-1/2} \text{ K}^{-1}$  (see also discussion below), and the thermal lightcurve amplitude would shrink to 1-2 mJy, well below the observed amplitude. The case of a dark Hi’iaka (and also Namaka) with  $p_V < 0.5$  can therefore be excluded. We should note here, that Namaka’s flux is only about 20 to 25% of Hi’iaka’s flux (for equal albedo), so excluding the case of a dark Namaka is much more difficult. The albedo limit of about 0.5 is not very well determined and it is related to the assumption of a beaming parameter of  $\eta = 1.0$ . A higher  $\eta$ -value (e.g.  $\eta=1.3$ ) for the satellites would lower the thermal emission contribution by 10-20% in the Herschel wavelength range (higher value for the shorter wavelengths). In this case, a Hi’iaka albedo of  $\sim 0.5$

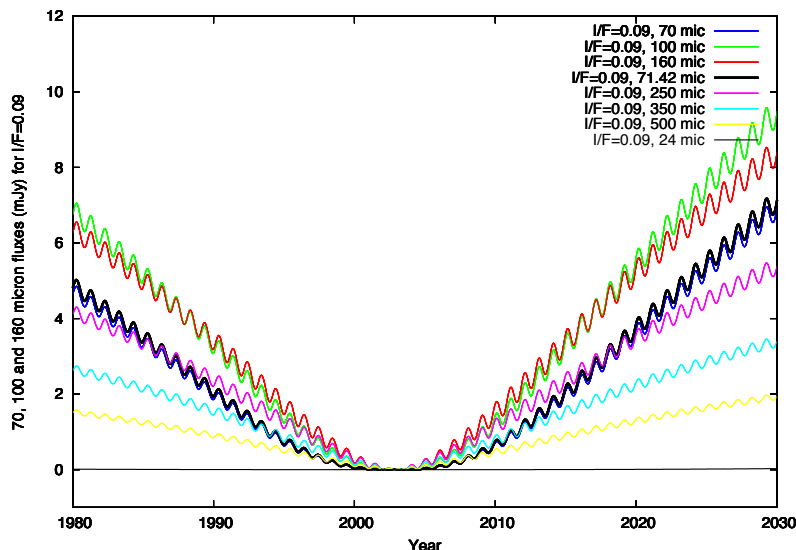


Figure 4: Thermal model flux predictions for Haumea’s ring for the time period 1980 to 2030. The Spitzer observations happened in 2005 and 2007 when the ring contribution was negligible. For the interpretation of the Herschel observations (2009-2011) we took the 0.4 to 1.4 mJy contribution into account, depending on the filter and observing time.

would still be compatible with the observed system fluxes. Additional small flux contributions could also come from undiscovered small satellites, but previous search programs (Brown et al. 2006) excluded other satellites at the size of Namaka or larger. However, the high albedo for the satellites is connected to small diameters of about 300 and 150 km for Hi’iaka and Namaka, respectively (see Table 2 and the discussions in Section 3.3). And since the masses are known, their densities must be well above  $1.0 \text{ g cm}^{-3}$  to comply with the mass and the brightness constraints. This makes these satellites (or at least Hi’iaka) very special in the current size-density picture (see Kiss et al. 2018). They show that all TNOs below 500 km in diameter seem to have densities well below  $1.0 \text{ g cm}^{-3}$ , i.e. close to (or even below) the density of pure water ice or granular ice with self-compression (Durham et al. 2005). The indication for higher densities for Haumea satellites points therefore to a formation process of these two satellites which is different from other small-size TNOs. A density below  $1.0 \text{ g cm}^{-3}$  would also be the expectation for Haumea’s satellites if they have been formed by a collision. Their density should represent the icy crust of Haumea which is expected to be much lower than Haumea’s bulk density of about  $1.9 \text{ g cm}^{-3}$ . These questions about Hi’iaka’s and Namaka’s density and their formation cannot be answered conclusively by our thermal measurements, especially, since the masses of both satellites are also uncertain (Ragozzine and Brown 2009).

The two constraints from Figs. 2 and 3 indicate that Haumea’s thermal inertia is very likely between  $2$  and  $10 \text{ J m}^{-2} \text{ s}^{-1/2} \text{ K}^{-1}$  (possibly up to  $15 \text{ J m}^{-2} \text{ s}^{-1/2} \text{ K}^{-1}$  if the a-axis is larger than the default value). This can be tested on all thermal data combined with a standard radiometric technique. In a first case (case I) we do not subtract any ring or satellite contribution. In case II and case III, we use all MIPS/PACS/SPIRE fluxes with the corresponding satellite (see Table 2) and ring contributions (see Table 3) subtracted. In case II, we assume a high albedo of  $p_V=0.8$  for both satellites (low satellite flux contribution), in case III we assume  $p_V=0.5$  (producing higher satellite flux contributions). Then we search for the thermal inertia that produces the best fit to all data simultaneously, without violating the occultation and H-mag constraints.

We summarized our results in Table 4. The  $\chi^2$  minima are not changing much for the three cases, but when studying the fits to the different thermal lightcurves individually, we see problems for low ( $< 3 \text{ J m}^{-2} \text{ s}^{-1/2} \text{ K}^{-1}$ ) and

Table 4: Radiometric analysis of all thermal measurements combined. Cases are explained in the text. We accepted values for the reduced  $\chi^2$  up to 1.4, with the optimum  $\chi^2$  around 0.7 (case I & II) and 0.8 (case III).

Case	TI range [J m <sup>2</sup> s <sup>1/2</sup> K <sup>1</sup> ]	comments
I	1-3	trend in obs/mod ratios with wavelengths, conflict with mass-brightness constraints on the satellites
II	2-7	best solution at TI=5 ( $\chi_r^2=0.7$ ) compatible with satellite mass/density estimates match to absolute flux level and lightcurve amplitude
III	7-11	amplitude fit and overall match to flux levels degrading, trend in obs/mod ratios with wavelengths

high ( $\Gamma > 8 \text{ J m}^{-2} \text{ s}^{-1/2} \text{ K}^{-1}$ ) thermal inertias. These problems are nicely visible in Figure 5 (bottom part) where the different solutions for the highest-quality PACS  $100 \mu\text{m}$  lightcurve are shown. Case I and case III also fail to match the lightcurve-averaged fluxes in different bands ( $70, 100, 160 \mu\text{m}$ ) equally well: In the observation-to-model ratios one can see a strong trend with wavelengths (the models overestimate the  $70 \mu\text{m}$  fluxes and underestimate the  $160 \mu\text{m}$  levels). Another argument against case I: The satellite mass estimates by Ragozzine and Brown (2009) lead to a thermal signal of at least 1-2 mJy in the PACS bands for the highest possible albedo and significantly more for a lower albedo (and/or in case of more, so-far undiscovered, satellites). The case I solution can therefore only produce a lower limit for Haumea’s thermal inertia. Case III is also very problematic: if the ring and the satellites contribute too much, then Haumea’s thermal inertia has to increase accordingly and this would lower the thermal lightcurve amplitude well below the observed level. The offset in observation-to-model ratio at sub-millimeter range would also increase and be more difficult to explain (see lower part of Figure 5).

The overall best solution (in reduced  $\chi^2$ , and also when inspecting the match to the absolute fluxes and thermal lightcurve), is found for case II, with TPM settings of  $\Gamma \sim 5$ , a phase integral of 0.65, and a surface roughness of  $\sim 0.2$  r.m.s. of surface slopes. Figure 5 shows our best match to the data for case II, with only the small ring/satellite contributions (5-20% to the total observed fluxes) subtracted. In the upper part of the figure we have calculated Haumea’s thermal emission at the given observing geometry for each thermal measurement, and we show the observations-to-model ratios as a function of wavelengths. At  $70, 100,$  and  $160 \mu\text{m}$ , the measurements are well matched, at  $24 \mu\text{m}$  the model prediction is in agreement with the non- or marginal detection, but at  $250$  and  $350 \mu\text{m}$  the predictions overestimate the fluxes. It seems that the ring and satellite contributions are negligible at these wavelengths, indicating that their sub-millimeter emissivity is lower than the assumed value of  $\epsilon = 0.9$  (for the satellites) and  $1.0$  (for the ring). Another option is a higher I/F value for the ring: with increasing albedo the thermal ring emission is going down and for an I/F of 0.5 it would decrease to about half the assumed value, but this would also lower the ring contribution in the PACS range and it would only partly explain the SPIRE data problem. But both effects combined would lower the sub-millimeter thermal contribution of the ring and the satellites and would bring the observation-to-model ratios at  $250$  and  $350 \mu\text{m}$  in Figure 5 closer to 1.0. Our current ring model does not depend on particle sizes and it is therefore not possible to constrain the particle sizes. However, a recent study on the particle dynamics of Haumea’s dust ring (Kovács and Regály 2018) found that particles with sizes of  $\sim 1 \mu\text{m}$  would accumulate circularly in a narrow ring near the 3:1 spin-orbit resonance and survive for a reasonable time periods. Such small grain sizes would make the ring more transparent at far-IR wavelengths and lead to a better match between our Haumea predictions and the (case II) fluxes.

How does Haumea’s thermal inertia compare with other distant TNOs or with large dwarf planets with known thermal properties? Lellouch et al. (2013) analyzed a large sample of TNOs and found a  $\Gamma = 2.5 \pm 0.5 \text{ J m}^{-2} \text{ s}^{-1/2} \text{ K}^{-1}$  for objects at heliocentric distances of  $r_{helio} = 20\text{--}50 \text{ AU}$ . Haumea is at  $r_{helio} = \sim 51 \text{ AU}$  and the thermal inertia should therefore be slightly lower due to the lower surface temperatures: assuming that the  $T^3$  term dominates in the thermal conductivity (the thermal inertia scales with  $\sim r^{3/4}$ ; see e.g. Delbo et al. 2015). On the other hand, the thermal inertia of Pluto and Charon are larger:  $\Gamma_{Pluto} = 16\text{--}26 \text{ J m}^{-2} \text{ s}^{-1/2} \text{ K}^{-1}$  and  $\Gamma_{Charon} = 9\text{--}14 \text{ J m}^{-2} \text{ s}^{-1/2} \text{ K}^{-1}$  (Lellouch et al. 2011, 2016). A Pluto(Charon)-like surface has then a thermal inertia of  $11.3\text{--}18.3(6.3\text{--}9.9) \text{ J m}^{-2} \text{ s}^{-1/2} \text{ K}^{-1}$  at the distance of

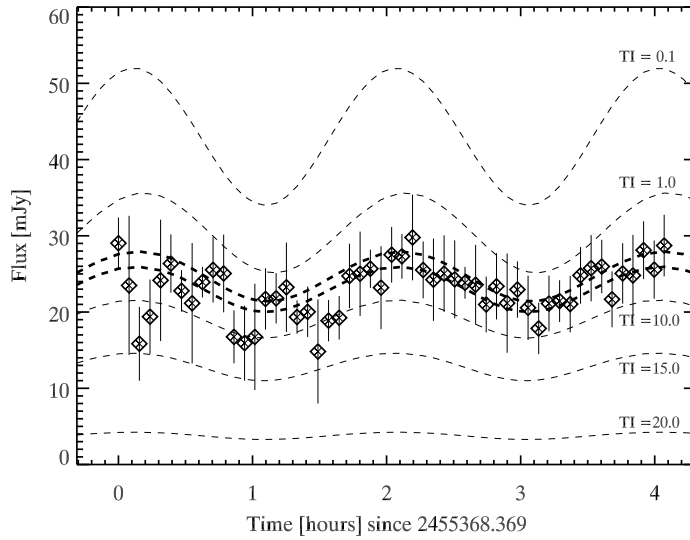
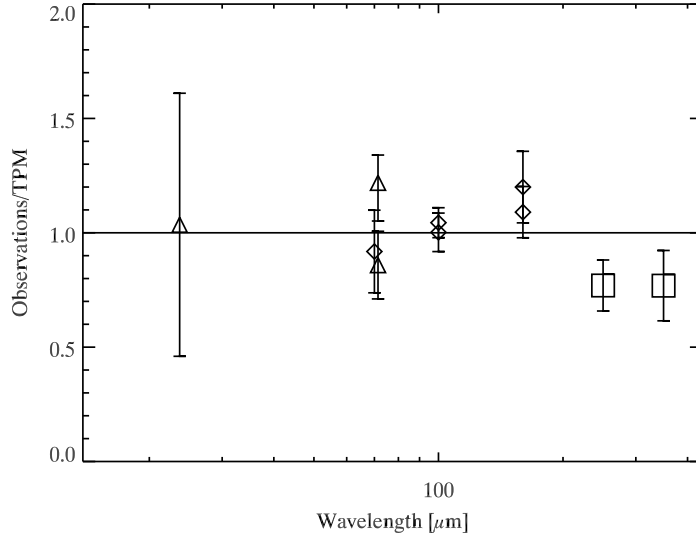


Figure 5: Top: All observations (MIPS and PACS lightcurves have been averaged), divided by the corresponding TPM predictions ( $\Gamma = 5 \text{ J m}^{-2} \text{ s}^{-1/2} \text{ K}^{-1}$ , r.m.s. of surface slopes of 0.2,  $q = 0.65$ , occultation-derived 3-D shape and spin properties for pole 1, Haumea emissivity of 0.9 in the PACS range and 0.8 in the SPIRE range). Triangles are Spitzer-MIPS data, diamonds are Herschel-PACS, and boxes are Herschel-SPIRE observations. Small thermal contributions (case II) from the ring and the satellites were subtracted from the observed fluxes. The  $24 \mu\text{m}$  data point is a non- or marginal detection, the  $70$ ,  $100$ , and  $160 \mu\text{m}$  points are well matched. At  $250$  and  $350 \mu\text{m}$  we might have overestimated the ring and satellite contributions (see text). Note that the true size, shape and spin properties have been used for the ratio calculations. Bottom: the most-accurate  $100 \mu\text{m}$  lightcurve (PACS, second epoch in Jun 2010), with minimum ring/satellite contributions subtracted (case II), shown together with absolute model predictions over-plotted. The two thicker dashed lines are related to  $\Gamma = 4 \text{ J m}^{-2} \text{ s}^{-1/2} \text{ K}^{-1}$  (higher one) and  $\Gamma = 6 \text{ J m}^{-2} \text{ s}^{-1/2} \text{ K}^{-1}$  (lower one).

Haumea (about a factor of 1.4 lower). But the high  $\Gamma$ -values for Pluto and Charon are thought to be caused by large diurnal skin depth due to their slow rotation ( $\sim P^{1/2}$  dependence; see also discussion in Kiss et al. 2018). Haumea rotates much faster than Pluto and Charon (6.38 d orbital/rotation period of Pluto-Charon versus 3.91 h for Haumea), and also faster than typical TNOs ( $P = \sim 6$ -12 h; Duffard et al. 2009; Thirouin et al. 2016). Taking the skin-depth effect into account would lower the expected thermal inertia to about 1.8-2.9(1.0-1.5)  $\text{J m}^{-2} \text{s}^{-1/2} \text{K}^{-1}$  for Haumea, if we assume a Pluto(Charon)-like surface. Our derived values for Haumea are a factor of 2-3 higher and point to a more compact (hence higher conductivity) surface than compared to Pluto or Charon.

The phase integral  $q$  is a critical property in the thermophysical model concept for high-albedo objects like Haumea. The thermal flux depends mainly on the object's size and its Bond albedo  $A_b$ , with  $A_b = p_V \cdot q$ . For objects with a standard scattering behavior in the visible, the phase slope  $G$  is given with 0.15, leading to a phase integral of  $q = 0.39$  (Bowell et al. 1989). This works well for low-albedo objects, but fails for high-albedo objects. Pluto's phase integral was found to be  $q = 0.8$  (Lellouch et al. 2000), which was used by Stansberry et al. (2008) for the interpretation of the Spitzer measurements of Haumea. Lellouch et al. (2010) adopted a phase integral  $q = 0.7$ , intermediate between those estimated for Pluto (0.8) and Charon (0.6) (Lellouch et al. 2000). Santos-Sanz et al. (2017) determined a high phase integral ( $>0.73$ ) for Haumea by matching an overestimated 100/160- $\mu\text{m}$  lightcurve amplitude. Using the phase integral formula by Brucker et al. (2009):  $q = 0.336 \cdot p_V + 0.479$ , we find  $q = 0.65$  (for  $p_V = 0.51$ ). We used different values for  $q$ , but there are simply too many unknowns in the system to constrain its value. Overall, we find better fits to the data for higher values ( $q=0.65$  to 0.8), the lower values ( $q=0.45$ ) would push Haumea's thermal inertia to larger values (above 10  $\text{J m}^{-2} \text{s}^{-1/2} \text{K}^{-1}$ ) and decrease the thermal lightcurve amplitudes too much. However, the combination of a low  $q$ -values (around 0.5) with a smooth surface (r.m.s.  $< 0.2$ ) would also lead to an acceptable solution with  $\Gamma = 5 \text{ J m}^{-2} \text{s}^{-1/2} \text{K}^{-1}$ , and in agreement with the observed flux and amplitude levels (see Fig. 2).

The study of the DRS via thermal data is very uncertain. In Figure 1 it is difficult to identify which of the 100  $\mu\text{m}$  maxima is higher, the errors are large, and the outliers at 40 mJy are difficult to judge. Following the DRS phasing in Santos-Sanz et al. (2017) and also in Gourgeot et al. (2016), the DRS is connected to the second maximum (at rotational phases around 0.6 in Fig. 1 or at 2.15 hours in Fig. 5, lower part). Lacerda et al. (2008) suggested three different DRS models with a darker region covering only a few percent of the maximum equatorial cross-sectional area, up to a model where a whole hemisphere has a darker albedo. A few percent change in albedo between the DRS and the rest of the surface can easily explain the two maxima in reflected light, with the DRS connected to the lower optical maximum, hence the higher thermal maximum. At Herschel/Spitzer wavelengths, also the thermal inertia plays a role, and if there is a variation in thermal inertia, this could either compensate an albedo effect or enhance it, and also surface roughness and phase integral play a role. But such an investigation would require a high-quality thermal lightcurve, close in time with an optical lightcurve to constrain the physical and thermal properties of the DRS region.

## 5. Conclusions and outlook

The previously published thermal lightcurves (Lellouch et al. 2010; Santos-Sanz et al. 2017) showed a very large amplitude which led to a misinterpretation of Haumea's thermal properties and systematically underestimated (by  $\sim 25\%$ ) radiometric sizes. We have reanalyzed the Spitzer and Herschel far-infrared and sub-millimeter observations from 2005 to 2011 with the latest reduction and calibration schemes, and a more elaborate sky background handling. The new multi-filter Herschel-PACS fluxes and thermal lightcurves are presented in Tables A.6, A.7, A.8, A.9. The corresponding background-eliminated Herschel-PACS maps are available from the HSA. All thermal observations are measurements of the combined Haumea-ring-satellite system and their interpretation requires to consider possible ring and satellite contributions. Only the thermal lightcurve amplitude (measured at 70, 100, and 160  $\mu\text{m}$ ) is connected to Haumea itself. We confirm the 3.91 h periodicity of the thermal lightcurve and we see that thermal and visual lightcurves are in phase.

We estimated the time-dependent ring fluxes by using a simple thermal model from Lellouch et al. (2017), based on ring properties of Saturn and Chariklo. During the Spitzer observations in 2005/2006 the ring emission was small (and almost negligible), but due to the opening of the ring plane, the ring contributed  $\sim 1$ -1.5 mJy to the measured Herschel signals in 2009-2011.



The mass and brightness estimates (Brown et al. 2006; Ragozzine and Brown 2009) for the two Haumea satellites Hi'iaka and Namaka are crucial for the interpretation of the thermal measurements. We calculated the far-IR fluxes for both satellites for a size-albedo range which is compatible with these constraints and under the assumption of a density range between 0.5 and 1.5 g cm<sup>-3</sup>. In case of a high density of 1.5 g cm<sup>-3</sup> (requiring a geometric albedo of ~0.8), the satellites add about 1-1.5 mJy to the observed flux. More moderate density assumptions (related to a lower albedo) lead to much higher satellite fluxes and cause severe problems in interpreting the remaining Haumea-only far-IR fluxes.

The key element for the re-interpretation of the Haumea measurements, however, is coming from a successful occultation measurement (Ortiz et al. 2017). It led to the discovery of the ring around Haumea, a highly-accurate ellipse fit to the multi-chord event (which happened very close to the lightcurve minimum), and allowed to reconstruct the objects size, shape, and spin-properties. We used the occultation-derived properties to take a closer look at the possible thermal and physical properties of Haumea and its two satellites. We find that Haumea has a thermal inertia of about 5 J m<sup>-2</sup> s<sup>-1/2</sup> K<sup>-1</sup> (in combination with a surface roughness r.m.s. = 0.2, a phase integral q = 0.65, and the pole 1 solution in Ortiz et al. 2017). A much smaller of the thermal inertia value would require that the ring and the satellite fluxes are completely negligible, a higher value would lower the thermal lightcurve amplitude below the observed values. A lower phase integral (q = 0.5) would push the solution to higher thermal inertia (up to about 10 J m<sup>-2</sup> s<sup>-1/2</sup> K<sup>-1</sup>), assuming a similar surface roughness. When the degree of surface roughness is varied from 0.0 (smooth) to 0.5 (see Fornasier et al. 2013) the derived value of Haumea's thermal inertia would also vary in the range between 3 and 10 J m<sup>-2</sup> s<sup>-1/2</sup> K<sup>-1</sup>, with the smooth surface connected to a lower thermal inertia value. The most extreme thermal inertia of about ~15 J m<sup>-2</sup> s<sup>-1/2</sup> K<sup>-1</sup> is found for a low phase integral (q<0.5) combined with a high surface roughness (r.m.s. > 0.5).

The satellites are very likely in the smaller size regime (~300 km diameter for Hi'iaka and ~150 km for Namaka) linked to a high albedo p<sub>V</sub> >> 0.5, and connected to an unexpectedly high density > 1 g cm<sup>-3</sup>. Lower albedo solutions would push their thermal emission to large values which are not compatible with the occultation-derived size-shape-spin and our radiometric thermal-inertia solution. Our fit to the sub-millimeter thermal measurements improves if we lower the emissivity of the ring (ε = 1.0 assumed) and the satellites for which we assumed ε = 0.9.

Haumea's ring contribution to the total thermal flux will increase significantly over the next decades (Figure 4). The JWST-MIRI imager sensitivities (about 1 μJy at 15 μm to about 10 μJy at 25.5 μm for a SNR of 10 in 10,000 sec) would be perfectly suitable to measure the ring-only fluxes, but the spatial resolution will not be sufficient to separate the ring from the main body. However, MIRI measurements would allow us to confirm Haumea's thermal properties from the thermal lightcurve amplitude and the shape of its spectral energy distribution. Then, in comparison with the Spitzer and Herschel data, the MIRI multi-filter data will provide a higher-quality characterization of the ring properties as a byproduct.

Measurements with JWST-MIRI will be very sensitive to the thermal properties of Haumea. Based on our best-fit TPM (Γ=5 J m<sup>-2</sup> s<sup>-1/2</sup> K<sup>-1</sup>, q=0.65, r.m.s. = 0.2) for Haumea we predicted fluxes in three long-wavelengths MIRI channels (see Table 5).

Table 5: JWST-MIRI predictions for Feb 1, 2022 at r<sub>helio</sub> = 50.18 au, Δ = 50.00 au, α = 1.1°, at a solar elongation of 100° when Haumea is visible for JWST. The first column in each band gives the average flux level, the second the lightcurve variations. Note that at shorter wavelengths below ~20 μm there is still a significant contribution from reflected light in MIRI bands. These predictions depend also on the phase integral (here: q = 0.65) and the surface roughness (here: r.m.s. = 0.2) and have therefor significant uncertainties.

Thermal inertia Γ [J m <sup>2</sup> s <sup>1/2</sup> K <sup>1</sup> ]	21.0 μm		25.5 μm	
	flx[μJy]	amp[μJy]	flx[μJy]	amp[μJy]
0.5	33	±6	230	± 46
2.0	21	±3	131	± 12
5.0	19	±3	110	± 10
10	10	±2	57	± 10

The MIRI imager sensitivities (SNR = 10 in 10,000 sec) are increasing from about 1 μJy at 15 μm to about 10 μJy at 25.5 μm. It will therefore be possible to obtain SNR well above 25 in 1000 sec in the 25.5 μm filter at all rotational

phases. A second, shorter-wavelength band (possibly at  $21\ \mu\text{m}$ ) will allow characterizing the spectral slope and help to disentangle the ring and satellite contributions. At shorter wavelength below  $\sim 20\ \mu\text{m}$  there are still strong contributions from reflected Sun light.

## Acknowledgement

The research leading to these results has received funding from the European Union's Horizon 2020 Research and Innovation Programme, under Grant Agreement no 687378. Funding from the Spanish grant AYA-2017-89637-R is acknowledged.

## Appendix A. Herschel-PACS photometric flux densities

We performed aperture photometry on the reduced, calibrated, and background eliminated final images. The fluxes were aperture corrected, color-corrected (correction factors 1.00, 0.98, and 0.99 at  $70.0$ ,  $100.0$ , and  $160.0\ \mu\text{m}$ , respectively). We also included the recommended 5% absolute flux error when we use PACS fluxes in radiometric calculations.

### Appendix A.1. Lightcurve measurements at $100\ \mu\text{m}$

At  $100\ \mu\text{m}$ , we merged always three repetitions (shifted by 1) before extracting the aperture photometry (first line: repetitions 1-3, second line 2-4, third line 3-5, etc.).

### Appendix A.2. Lightcurve measurements at $160\ \mu\text{m}$

At  $160\ \mu\text{m}$ , we merged always six repetitions (shifted by 3) before extracting the aperture photometry (first line: repetitions 1-6, second line 4-9, third line 7-12, etc.).

### Appendix A.3. Multi-filter measurements

## References

- Balog, Z., Müller, T., Nielbock, M., Altieri, B., Klaas, U., Blommaert, J., Linz, H., Lutz, D., Moór, A., Billot, N., Sauvage, M., Okumura, K., Jul. 2014. The Herschel-PACS photometer calibration. Point-source flux calibration for scan maps. *Experimental Astronomy* 37, 129–160.
- Barkume, K. M., Brown, M. E., Schaller, E. L., Mar. 2006. Water Ice on the Satellite of Kuiper Belt Object 2003 EL<sub>61</sub>. *ApJ*640, L87–L89.
- Bowell, E., Hapke, B., Domingue, D., Lumme, K., Peltoniemi, J., Harris, A. W., 1989. Application of photometric models to asteroids. In: Binzel, R. P., Gehrels, T., Matthews, M. S. (Eds.), *Asteroids II*. pp. 524–556.
- Braga-Ribas, F., Sicardy, B., Ortiz, J. L., Snodgrass, C., Roques, F., Vieira-Martins, R., Camargo, J. I. B., Assafin, M., Duffard, R., Jehin, E., Pollock, J., Leiva, R., Emilio, M., Machado, D. I., Colazo, C., Lellouch, E., Skottfelt, J., Gillon, M., Ligier, N., Maquet, L., Benedetti-Rossi, G., Gomes, A. R., Kervella, P., Monteiro, H., Sfair, R., El Moutamid, M., Tancredi, G., Spagnotto, J., Maury, A., Morales, N., Gil-Hutton, R., Roland, S., Ceretta, A., Gu, S.-H., Wang, X.-B., Harpsøe, K., Rabus, M., Manfroid, J., Opitom, C., Vanzi, L., Mehret, L., Lorenzini, L., Schneiter, E. M., Melia, R., Lecacheux, J., Colas, F., Vachier, F., Widemann, T., Almenares, L., Sandness, R. G., Char, F., Perez, V., Lemos, P., Martinez, N., Jørgensen, U. G., Dominik, M., Roig, F., Reichart, D. E., Lacluyze, A. P., Haislip, J. B., Ivarsen, K. M., Moore, J. P., Frank, N. R., Lambas, D. G., Apr. 2014. A ring system detected around the Centaur (10199) Chariklo. *Nature*508, 72–75.
- Brown, M. E., Barkume, K. M., Ragozzine, D., Schaller, E. L., Mar. 2007. A collisional family of icy objects in the Kuiper belt. *Nature*446, 294–296.
- Brown, M. E., Bouchez, A. H., Rabinowitz, D., Sari, R., Trujillo, C. A., van Dam, M., Campbell, R., Chin, J., Hartman, S., Johansson, E., Lafon, R., Le Mignant, D., Stomski, P., Summers, D., Wizinowich, P., Oct. 2005. Keck Observatory Laser Guide Star Adaptive Optics Discovery and Characterization of a Satellite to the Large Kuiper Belt Object 2003 EL<sub>61</sub>. *ApJ*632, L45–L48.
- Brown, M. E., van Dam, M. A., Bouchez, A. H., Le Mignant, D., Campbell, R. D., Chin, J. C. Y., Conrad, A., Hartman, S. K., Johansson, E. M., Lafon, R. E., Rabinowitz, D. L., Stomski, Jr., P. J., Summers, D. M., Trujillo, C. A., Wizinowich, P. L., Mar. 2006. Satellites of the Largest Kuiper Belt Objects. *ApJ*639, L43–L46.
- Brucker, M. J., Grundy, W. M., Stansberry, J. A., Spencer, J. R., Sheppard, S. S., Chiang, E. I., Buie, M. W., May 2009. High albedos of low inclination Classical Kuiper belt objects. *Icarus*201, 284–294.
- Delbo, M., Mueller, M., Emery, J. P., Rozitis, B., Capria, M. T., 2015. Asteroid Thermophysical Modeling. pp. 107–128.
- Duffard, R., Ortiz, J. L., Thirouin, A., Santos-Sanz, P., Morales, N., Oct. 2009. Transneptunian objects and Centaurs from light curves. *A&A*505, 1283–1295.
- Durham, W. B., McKinnon, W. B., Stern, L. A., Sep. 2005. Cold compaction of water ice. *Geophys. Res. Lett.*32, L18202.
- Fornasier, S., Lellouch, E., Müller, T., Santos-Sanz, P., Panuzzo, P., Kiss, C., Lim, T., Mommert, M., Bockelée-Morvan, D., Vilenius, E., Stansberry, J., Tozzi, G. P., Mottola, S., Delsanti, A., Crovisier, J., Duffard, R., Henry, F., Lacerda, P., Barucci, A., Gicquel, A., Jul. 2013. TNOs are Cool: A survey of the trans-Neptunian region. VIII. Combined Herschel PACS and SPIRE observations of nine bright targets at  $70\text{--}500\ \mu\text{m}$ . *A&A*555, A15.

Table A.6: Herschel-PACS lightcurve observations (OBSIDs 1342188470, 1342188520) at 100  $\mu\text{m}$  on 2009 Dec 23. The times are observation mid-times in the Herschel reference frame.

mid-time obs. epoch	in-band flux & error [mJy]	abs. flux & error [mJy]	abs. flux & error [mJy]	abs. flux & error [mJy]
2455188.7492	25.49	9.37	26.01	9.46
2455188.7527	25.06	9.04	25.57	9.12
2455188.7562	23.55	8.96	24.03	9.04
2455188.7597	29.47	10.68	30.07	10.78
2455188.7632	34.11	7.85	34.81	8.03
2455188.7667	34.81	6.02	35.52	6.27
2455188.7702	32.41	6.33	33.07	6.53
2455188.7737	31.02	7.81	31.65	7.96
2455188.7772	26.47	8.16	27.01	8.27
2455188.7807	23.51	6.91	23.99	7.01
2455188.7842	18.59	4.91	18.97	5.00
2455188.7877	18.91	5.97	19.30	6.05
2455188.7912	17.76	6.18	18.12	6.24
2455188.7947	18.16	6.90	18.54	6.96
2455188.7982	23.24	5.33	23.72	5.46
2455188.8017	24.53	5.53	25.03	5.67
2455188.8052	25.69	5.71	26.22	5.86
2455188.8087	20.00	5.84	20.40	5.92
2455188.8122	21.57	5.84	22.01	5.94
2455188.8156	18.31	6.77	18.69	6.83
2455188.8191	22.52	4.71	22.98	4.84
2455188.8226	23.10	4.88	23.57	5.02
2455188.8261	28.57	4.01	29.15	4.26
2455188.8296	26.15	5.29	26.69	5.45
2455188.8331	23.01	5.68	23.48	5.80
2455188.8366	21.25	5.29	21.68	5.39
2455188.8401	24.08	5.72	24.57	5.84
2455188.8436	40.97	3.67	41.80	4.21
2455188.8471	42.61	5.39	43.48	5.79
2455188.8506	44.43	3.78	45.34	4.38
2455188.8541	26.61	5.49	27.15	5.65
2455188.8576	23.39	4.83	23.86	4.97
2455188.8611	18.93	4.99	19.32	5.08
2455188.8646	22.14	4.99	22.59	5.11
2455188.8681	25.24	5.06	25.76	5.22
2455188.8716	27.79	5.84	28.35	6.01
2455188.8751	20.83	6.74	21.26	6.82
2455188.8784	20.01	6.40	20.42	6.48

Fraser, W. C., Brown, M. E., Apr. 2009. NICMOS Photometry of the Unusual Dwarf Planet Haumea and its Satellites. *ApJ*695, L1–L3.

Gourgeot, F., Carry, B., Dumas, C., Vachier, F., Merlin, F., Lacerda, P., Barucci, M. A., Berthier, J., Aug. 2016. Near-infrared spatially resolved spectroscopy of (136108) Haumea’s multiple system. *A&A*593, A19.

Griffin, M. J., Abergel, A., Abreu, A., Ade, P. A. R., André, P., Augueres, J.-L., Babbedge, T., Bae, Y., Baillie, T., Baluteau, J.-P., Barlow, M. J., Bendo, G., Benielli, D., Bock, J. J., Bonhomme, P., Brisbin, D., Brockley-Blatt, C., Caldwell, M., Cara, C., Castro-Rodriguez, N., Cerulli, R., Chaniãl, P., Chen, S., Clark, E., Clements, D. L., Clerc, L., Coker, J., Communal, D., Conversi, L., Cox, P., Crumb, D., Cunningham, C., Daly, F., Davis, G. R., de Antoni, P., Delderfield, J., Devin, N., di Giorgio, A., Didschuns, I., Dohlen, K., Donati, M., Dowell, A., Dowell, C. D., Duband, L., Dumaye, L., Emery, R. J., Ferlet, M., Ferrand, D., Fontignie, J., Fox, M., Franceschini, A., Frerking, M., Fulton, T., Garcia, J.,

- Gastaud, R., Gear, W. K., Glenn, J., Goizel, A., Griffin, D. K., Grundy, T., Guest, S., Guillemet, L., Hargrave, P. C., Harwit, M., Hastings, P., Hatziminaoglou, E., Herman, M., Hinde, B., Hristov, V., Huang, M., Imhof, P., Isaak, K. J., Israelsson, U., Ivison, R. J., Jennings, D., Kiernan, B., King, K. J., Lange, A. E., Latter, W., Laurent, G., Laurent, P., Leeks, S. J., Lellouch, E., Levenson, L., Li, B., Li, J., Lilienthal, J., Lim, T., Liu, S. J., Lu, N., Madden, S., Mainetti, G., Marliani, P., McKay, D., Mercier, K., Molinari, S., Morris, H., Moseley, H., Mulder, J., Mur, M., Naylor, D. A., Nguyen, H., O'Halloran, B., Oliver, S., Olofsson, G., Olofsson, H.-G., Orfei, R., Page, M. J., Pain, I., Panuzzo, P., Papageorgiou, A., Parks, G., Parr-Burman, P., Pearce, A., Pearson, C., Pérez-Fournon, I., Pinsard, F., Pisano, G., Podosek, J., Pohlen, M., Polehampton, E. T., Poulliquen, D., Rigopoulou, D., Rizzo, D., Roseboom, I. G., Roussel, H., Rowan-Robinson, M., Rownd, B., Saraceno, P., Sauvage, M., Savage, R., Savini, G., Sawyer, E., Scharnberg, C., Schmitt, D., Schneider, N., Schulz, B., Schwartz, A., Shafer, R., Shupe, D. L., Sibthorpe, B., Sidher, S., Smith, A., Smith, A. J., Smith, D., Spencer, L., Stobie, B., Sudiwala, R., Sukhatme, K., Surace, C., Stevens, J. A., Swinyard, B. M., Trichas, M., Tourette, T., Triou, H., Tseng, S., Tucker, C., Turner, A., Vaccari, M., Valtchanov, I., Vigroux, L., Virique, E., Voellmer, G., Walker, H., Ward, R., Waskett, T., Weilert, M., Wesson, R., White, G. J., Whitehouse, N., Wilson, C. D., Winter, B., Woodcraft, A. L., Wright, G. S., Xu, C. K., Zavagno, A., Zmiev, M., Zhang, L., Zonca, E., Jul. 2010. The Herschel-SPIRE instrument and its in-flight performance. *A&A*518, L3.
- Harris, A. W., Feb. 1998. A Thermal Model for Near-Earth Asteroids. *Icarus*131, 291–301.
- Kiss, C., Marton, G., Parker, A. H., Gundy, W., Farkas-Takács, A., Stansberry, J. Pál, A., Müller, T., Noll, K. S., Schwamb, M. E., Barr, A. C., Young, L. A., Vinkó, J., 2018. The mass and density of the dwarf planet (225088) 2007 OR<sub>10</sub>. *Icarus* submitted.
- Kiss, C., Müller, T. G., Vilenius, E., Pál, A., Santos-Sanz, P., Lellouch, E., Marton, G., Verebelyi, E., Szalai, N., Hartogh, P., Stansberry, J., Henry, F., Delsanti, A., Jul. 2014. Optimized Herschel/PACS photometer observing and data reduction strategies for moving solar system targets. *Experimental Astronomy* 37, 161–174.
- Klaas, U., Balog, Z., Nielbock, M., Müller, T. G., Linz, H., Kiss, C., May 2018. Herschel-PACS photometry of faint stars for sensitivity performance assessment and establishment of faint FIR primary photometric standards. *A&A*613, A40.
- Kovács, T., Regály, Z., Oct. 2018. Dynamics of Haumea's dust ring. *MNRAS*479, 4560–4565.
- Lacerda, P., Feb. 2009. Time-Resolved Near-Infrared Photometry of Extreme Kuiper Belt Object Haumea. *AJ*137, 3404–3413.
- Lacerda, P., Jewitt, D., Peixinho, N., May 2008. High-Precision Photometry of Extreme KBO 2003 EL<sub>61</sub>. *AJ*135, 1749–1756.
- Lagerros, J. S. V., Jun. 1996. Thermal physics of asteroids. I. Effects of shape, heat conduction and beaming. *A&A*310, 1011–1020.
- Lagerros, J. S. V., Sep. 1997. Thermal physics of asteroids. III. Irregular shapes and albedo variegations. *A&A*325, 1226–1236.
- Lagerros, J. S. V., Apr. 1998. Thermal physics of asteroids. IV. Thermal infrared beaming. *A&A*332, 1123–1132.
- Lellouch, E., Kiss, C., Santos-Sanz, P., Müller, T. G., Fornasier, S., Groussin, O., Lacerda, P., Ortiz, J. L., Thirouin, A., Delsanti, A., Duffard, R., Harris, A. W., Henry, F., Lim, T., Moreno, R., Mommert, M., Mueller, M., Protopapa, S., Stansberry, J., Trilling, D., Vilenius, E., Barucci, A., Crovisier, J., Doressoundiram, A., Dotto, E., Gutiérrez, P. J., Hainaut, O., Hartogh, P., Hestroffer, D., Horner, J., Jorda, L., Kidger, M., Lara, L., Rengel, M., Swinyard, B., Thomas, N., Jul. 2010. "TNOs are cool": A survey of the trans-Neptunian region. II. The thermal lightcurve of (136108) Haumea. *A&A*518, L147.
- Lellouch, E., Laureijs, R., Schmitt, B., Quirico, E., de Bergh, C., Crovisier, J., Coustenis, A., Sep. 2000. Pluto's Non-isothermal Surface. *Icarus*147, 220–250.
- Lellouch, E., Moreno, R., Müller, T., Fornasier, S., Santos-Sanz, P., Moullet, A., Gurwell, M., Stansberry, J., Leiva, R., Sicardy, B., Butler, B., Boissier, J., Dec. 2017. The thermal emission of Centaurs and trans-Neptunian objects at millimeter wavelengths from ALMA observations. *A&A*608, A45.
- Lellouch, E., Santos-Sanz, P., Fornasier, S., Lim, T., Stansberry, J., Vilenius, E., Kiss, C., Müller, T., Marton, G., Protopapa, S., Panuzzo, P., Moreno, R., Apr. 2016. The long-wavelength thermal emission of the Pluto-Charon system from Herschel observations. Evidence for emissivity effects. *A&A*588, A2.
- Lellouch, E., Santos-Sanz, P., Lacerda, P., Mommert, M., Duffard, R., Ortiz, J. L., Müller, T. G., Fornasier, S., Stansberry, J., Kiss, C., Vilenius, E., Mueller, M., Peixinho, N., Moreno, R., Groussin, O., Delsanti, A., Harris, A. W., Sep. 2013. "TNOs are Cool": A survey of the trans-Neptunian region. IX. Thermal properties of Kuiper belt objects and Centaurs from combined Herschel and Spitzer observations. *A&A*557, A60.
- Lellouch, E., Stansberry, J., Emery, J., Grundy, W., Cruikshank, D. P., Aug. 2011. Thermal properties of Pluto's and Charon's surfaces from Spitzer observations. *Icarus*214, 701–716.
- Lockwood, A. C., Brown, M. E., Stansberry, J., May 2014. The Size and Shape of the Oblong Dwarf Planet Haumea. *Earth Moon and Planets* 111, 127–137.
- Merlin, F., Guilbert, A., Dumas, C., Barucci, M. A., de Bergh, C., Vernazza, P., May 2007. Properties of the icy surface of the TNO 136108 (2003 EL<sub>61</sub>). *A&A*466, 1185–1188.
- Müller, T. G., Dec. 2002. Thermophysical analysis of infrared observations of asteroids. *Meteoritics and Planetary Science* 37, 1919–1928.
- Müller, T. G., Lagerros, J. S. V., Oct. 1998. Asteroids as far-infrared photometric standards for ISOPHOT. *A&A*338, 340–352.
- Müller, T. G., Lellouch, E., Bönhardt, H., Stansberry, J., Barucci, A., Crovisier, J., Delsanti, A., Doressoundiram, A., Dotto, E., Duffard, R., Fornasier, S., Groussin, O., Gutiérrez, P. J., Hainaut, O., Harris, A. W., Hartogh, P., Hestroffer, D., Horner, J., Jewitt, D., Kidger, M., Kiss, C., Lacerda, P., Lara, L., Lim, T., Mueller, M., Moreno, R., Ortiz, J.-L., Rengel, M., Santos-Sanz, P., Swinyard, B., Thomas, N., Thirouin, A., Trilling, D., Sep. 2009. TNOs are Cool: A Survey of the Transneptunian Region. *Earth Moon and Planets* 105, 209–219.
- Ortiz, J. L., Santos-Sanz, P., Sicardy, B., Benedetti-Rossi, G., Bérard, D., Morales, N., Duffard, R., Braga-Ribas, F., Hopp, U., Ries, C., Nascimbeni, V., Marzari, F., Granata, V., Pál, A., Kiss, C., Pribulla, T., Komžík, R., Hornoch, K., Pravec, P., Bacci, P., Mastrapieri, M., Nerli, L., Mazzei, L., Bachini, M., Martinelli, F., Succi, G., Ciabattari, F., Mikuz, H., Carbognani, A., Gaehrken, B., Mottola, S., Hellmich, S., Rommel, F. L., Fernández-Valenzuela, E., Campo Bagatin, A., Cikota, S., Cikota, A., Lecacheux, J., Vieira-Martins, R., Camargo, J. I. B., Assafin, M., Colas, F., Behrend, R., Desmars, J., Meza, E., Alvarez-Candal, A., Beisker, W., Gomes-Junior, A. R., Morgado, B. E., Roques, F., Vachier, F., Berthier, J., Mueller, T. G., Madio, J. M., Unsalan, O., Sonbas, E., Karaman, N., Erece, O., Koseoglu, D. T., Ozisik, T., Kalkan, S., Guney, Y., Niaei, M. S., Satir, O., Yesilyaprak, C., Puskullu, C., Kabas, A., Demircan, O., Alikakos, J., Charmandaris, V., Leto, G., Ohlert, J., Christille, J. M., Szakáts, R., Takácsné Farkas, A., Varga-Verebelyi, E., Marton, G., Marciniak, A., Bartczak, P., Santana-Ros, T., Butkiewicz-Bąk, M., Dudziński, G., Alí-Lagoa, V., Gazeas, K., Tzouganas, L., Paschalis, N., Tsamis, V., Sánchez-Lavega, A., Pérez-Hoyos, S., Hueso, R., Guirado, J. C., Peris, V., Iglesias-Marzoa, R., Oct. 2017. The size, shape, density and ring of the dwarf planet Haumea from a stellar occultation. *Nature*550, 219–223.
- Ortiz, J. L., Sicardy, B., Braga-Ribas, F., Alvarez-Candal, A., Lellouch, E., Duffard, R., Pinilla-Alonso, N., Ivanov, V. D., Littlefair, S. P., Camargo,

- J. I. B., Assafin, M., Unda-Sanzana, E., Jehin, E., Morales, N., Tancredi, G., Gil-Hutton, R., de La Cueva, I., Colque, J. P., da Silva Neto, D. N., Manfroid, J., Thirouin, A., Gutiérrez, P. J., Lecacheux, J., Gillon, M., Maury, A., Colas, F., Licandro, J., Mueller, T., Jacques, C., Weaver, D., Milone, A., Salvo, R., Bruzzone, S., Organero, F., Behrend, R., Roland, S., Vieira-Martins, R., Widemann, T., Roques, F., Santos-Sanz, P., Hestroffer, D., Dhillon, V. S., Marsh, T. R., Harlinton, C., Campo Bagatin, A., Alonso, M. L., Ortiz, M., Colazo, C., Lima, H. J. F., Oliveira, A. S., Kerber, L. O., Smiljanic, R., Pimentel, E., Giacchini, B., Casella, P., Emilio, M., Nov. 2012. Albedo and atmospheric constraints of dwarf planet Makemake from a stellar occultation. *Nature*491, 566–569.
- Pilbratt, G. L., Riedinger, J. R., Passvogel, T., Crone, G., Doyle, D., Gageur, U., Heras, A. M., Jewell, C., Metcalfe, L., Ott, S., Schmidt, M., Jul. 2010. Herschel Space Observatory. An ESA facility for far-infrared and submillimetre astronomy. *A&A*518, L1.
- Pinilla-Alonso, N., Brunetto, R., Licandro, J., Gil-Hutton, R., Roush, T. L., Strazzulla, G., Mar. 2009. The surface of (136108) Haumea (2003 EL<sub>61</sub>), the largest carbon-depleted object in the trans-Neptunian belt. *A&A*496, 547–556.
- Poglitsch, A., Waelkens, C., Geis, N., Feuchtgruber, H., Vandenbussche, B., Rodriguez, L., Krause, O., Renotte, E., van Hoof, C., Saraceno, P., Cepa, J., Kerschbaum, F., Agnès, P., Ali, B., Altieri, B., Andreani, P., Augueres, J.-L., Balog, Z., Barl, L., Bauer, O. H., Belbachir, N., Benedettini, M., Billot, N., Boulade, O., Bischof, H., Blommaert, J., Callut, E., Cara, C., Cerulli, R., Cesarsky, D., Contursi, A., Creten, Y., De Meester, W., Doublier, V., Doumayrou, E., Duband, L., Exter, K., Genzel, R., Gillis, J.-M., Grözinger, U., Henning, T., Herreros, J., Huygen, R., Inguascio, M., Jakob, G., Jamar, C., Jean, C., de Jong, J., Katterloher, R., Kiss, C., Klaas, U., Lemke, D., Lutz, D., Madden, S., Marquet, B., Martignac, J., Mazy, A., Merken, P., Montfort, F., Morbidelli, L., Müller, T., Nielbock, M., Okumura, K., Orfei, R., Ottensamer, R., Pezzuto, S., Popesso, P., Putzeys, J., Regibo, S., Reveret, V., Royer, P., Sauvage, M., Schreiber, J., Stegmaier, J., Schmitt, D., Schubert, J., Sturm, E., Thiel, M., Tofani, G., Vavrek, R., Wetzstein, M., Wieprecht, E., Wiezorrek, E., Jul. 2010. The Photodetector Array Camera and Spectrometer (PACS) on the Herschel Space Observatory. *A&A*518, L2.
- Rabinowitz, D., Tourtellotte, S., Brown, M., Trujillo, C., Aug. 2005. Photometric observations of a very bright TNO with an extraordinary lightcurve. In: *AAS/Division for Planetary Sciences Meeting Abstracts #37*. Vol. 37 of *Bulletin of the American Astronomical Society*. p. 746.
- Rabinowitz, D. L., Barkume, K., Brown, M. E., Roe, H., Schwartz, M., Tourtellotte, S., Trujillo, C., Mar. 2006. Photometric Observations Constraining the Size, Shape, and Albedo of 2003 EL<sub>61</sub>, a Rapidly Rotating, Pluto-sized Object in the Kuiper Belt. *ApJ*639, 1238–1251.
- Ragozzine, D., Brown, M. E., Jun. 2009. Orbits and Masses of the Satellites of the Dwarf Planet Haumea (2003 EL<sub>61</sub>). *AJ*137, 4766–4776.
- Rieke, G. H., Young, E. T., Engelbracht, C. W., Kelly, D. M., Low, F. J., Haller, E. E., Beeman, J. W., Gordon, K. D., Stansberry, J. A., Misselt, K. A., Cadien, J., Morrison, J. E., Rivlis, G., Latter, W. B., Noriega-Crespo, A., Padgett, D. L., Stapelfeldt, K. R., Hines, D. C., Egami, E., Muzerolle, J., Alonso-Herrero, A., Blaylock, M., Dole, H., Hinz, J. L., Le Floc'h, E., Papovich, C., Pérez-González, P. G., Smith, P. S., Su, K. Y. L., Bennett, L., Frayer, D. T., Henderson, D., Lu, N., Masci, F., Pesenson, M., Rebull, L., Rho, J., Keene, J., Stolovy, S., Wachter, S., Wheaton, W., Werner, M. W., Richards, P. L., Sep. 2004. The Multiband Imaging Photometer for Spitzer (MIPS). *ApJS*154, 25–29.
- Santos-Sanz, P., Lellouch, E., Groussin, O., Lacerda, P., Müller, T. G., Ortiz, J. L., Kiss, C., Vilenius, E., Stansberry, J., Duffard, R., Fornasier, S., Jorda, L., Thirouin, A., Aug. 2017. “TNOs are Cool”: A survey of the trans-Neptunian region. XII. Thermal light curves of Haumea, 2003 VS<sub>2</sub> and 2003 AZ<sub>84</sub> with Herschel/PACS. *A&A*604, A95.
- Stansberry, J., Grundy, W., Brown, M., Cruikshank, D., Spencer, J., Trilling, D., Margot, J.-L., 2008. Physical Properties of Kuiper Belt and Centaur Objects: Constraints from the Spitzer Space Telescope. pp. 161–179.
- Stansberry, J. A., Gordon, K. D., Bhattacharya, B., Engelbracht, C. W., Rieke, G. H., Marleau, F. R., Fadda, D., Frayer, D. T., Noriega-Crespo, A., Wachter, S., Young, E. T., Müller, T. G., Kelly, D. M., Blaylock, M., Henderson, D., Neugebauer, G., Beeman, J. W., Haller, E. E., Sep. 2007. Absolute Calibration and Characterization of the Multiband Imaging Photometer for Spitzer. III. An Asteroid-based Calibration of MIPS at 160  $\mu$ m. *PASP*119, 1038–1051.
- Tegler, S. C., Grundy, W. M., Romanishin, W., Consolmagno, G. J., Mogren, K., Vilas, F., Feb. 2007. Optical Spectroscopy of the Large Kuiper Belt Objects 136472 (2005 FY9) and 136108 (2003 EL<sub>61</sub>). *AJ*133, 526–530.
- Thirouin, A., 2013. Study of transneptunian objects using photometrics techniques and numerical simulations. Doctoral Dissertation (available from <http://hdl.handle.net/10481/30832>).
- Thirouin, A., Sheppard, S. S., Noll, K. S., Moskovitz, N. A., Ortiz, J. L., Doressoundiram, A., Jun. 2016. Rotational Properties of the Haumea Family Members and Candidates: Short-term Variability. *AJ*151, 148.
- Trujillo, C. A., Brown, M. E., Barkume, K. M., Schaller, E. L., Rabinowitz, D. L., Feb. 2007. The Surface of 2003 EL<sub>61</sub> in the Near-Infrared. *ApJ*655, 1172–1178.
- Vilenius, E., Stansberry, J., Müller, T., Mueller, M., Kiss, C., Santos-Sanz, P., Mommert, M., Pál, A., Lellouch, E., Ortiz, J. L., Peixinho, N., Thirouin, A., Lykawka, P. S., Horner, J., Duffard, R., Fornasier, S., Delsanti, A., Oct. 2018. “TNOs are Cool”: A survey of the trans-Neptunian region. XIII. Size/albedo characterization of the Haumea family observed with Herschel and Spitzer. *A&A*618, A136.
- Werner, M. W., Roellig, T. L., Low, F. J., Rieke, G. H., Rieke, M., Hoffmann, W. F., Young, E., Houck, J. R., Brandl, B., Fazio, G. G., Hora, J. L., Gehrz, R. D., Helou, G., Soifer, B. T., Stauffer, J., Keene, J., Eisenhardt, P., Gallagher, D., Gautier, T. N., Irace, W., Lawrence, C. R., Simmons, L., Van Cleve, J. E., Jura, M., Wright, E. L., Cruikshank, D. P., Sep. 2004. The Spitzer Space Telescope Mission. *ApJS*154, 1–9.

Table A.7: Herschel-PACS lightcurve observations (OBSIDs 1342198851, 1342198905/906) at  $100\ \mu\text{m}$  on 2010 Jun 20/21. The times are observation mid-times in the Herschel reference frame.

mid-time obs. epoch	in-band flux & error [mJy]	abs. flux & error [mJy]	abs. flux & error [mJy]	abs. flux & error [mJy]
2455368.3690	31.39	2.99	32.03	3.38
2455368.3723	25.96	9.04	26.49	9.13
2455368.3755	18.46	4.75	18.84	4.84
2455368.3788	21.94	4.76	22.39	4.88
2455368.3821	26.62	7.85	27.16	7.96
2455368.3853	28.77	3.54	29.36	3.82
2455368.3886	25.27	2.44	25.78	2.74
2455368.3919	23.67	7.81	24.15	7.90
2455368.3951	26.38	1.52	26.92	2.01
2455368.3984	27.97	4.05	28.54	4.29
2455368.4017	27.50	4.91	28.06	5.10
2455368.4049	19.36	3.33	19.75	3.47
2455368.4082	18.54	4.83	18.92	4.92
2455368.4114	19.34	6.90	19.74	6.97
2455368.4147	24.22	3.83	24.71	4.02
2455368.4180	24.30	3.07	24.80	3.30
2455368.4212	25.73	5.71	26.25	5.86
2455368.4245	21.89	1.90	22.34	2.19
2455368.4278	22.57	3.11	23.03	3.31
2455368.4310	17.46	6.77	17.82	6.83
2455368.4343	21.44	2.49	21.87	2.71
2455368.4376	21.81	2.65	22.25	2.86
2455368.4408	27.18	4.01	27.73	4.23
2455368.4441	27.46	5.36	28.02	5.53
2455368.4473	28.11	2.08	28.68	2.51
2455368.4506	25.68	5.29	26.20	5.44
2455368.4539	29.91	3.33	30.52	3.65
2455368.4571	29.70	2.52	30.31	2.93
2455368.4604	32.12	5.39	32.78	5.62
2455368.4637	27.95	3.46	28.52	3.73
2455368.4669	26.69	5.23	27.24	5.40
2455368.4702	27.48	4.83	28.04	5.02
2455368.4735	26.75	4.93	27.29	5.11
2455368.4767	26.30	1.61	26.83	2.08
2455368.4800	26.05	5.06	26.58	5.23
2455368.4833	23.51	3.47	23.99	3.66
2455368.4865	25.86	4.15	26.38	4.35
2455368.4898	23.69	6.40	24.17	6.51
2455368.4930	25.44	3.47	25.95	3.69
2455368.4963	23.09	4.06	23.56	4.22
2455368.4996	20.43	3.21	20.85	3.37
2455368.5028	23.64	3.47	24.12	3.66
2455368.5061	23.94	2.46	24.43	2.74
2455368.5094	23.56	3.51	24.04	3.70
2455368.5126	27.26	3.47	27.81	3.72
2455368.5159	28.18	4.11	28.75	4.35
2455368.5192	28.39	3.20	28.97	3.50
2455368.5224	24.18	3.47	24.67	3.67
2455368.5257	27.50	3.73	28.06	3.97
2455368.5289	27.24	5.14	27.80	5.32
2455368.5322	30.50	3.47	31.12	3.79
2455368.5355	28.00	3.55	28.57	3.82
2455368.5386	31.09	3.73	31.72	4.04

Table A.8: Herschel-PACS lightcurve observations at  $160\mu\text{m}$  on 2009 Dec 23 (OBSIDs 1342188470, 1342188520) and 2010 Jun 20/21 (OBSIDs 1342198851, 1342198905/906). The times are observation mid-times in the Herschel reference frame.

mid-time obs. epoch	in-band flux & error [mJy]	abs. flux & error [mJy]	abs. flux & error [mJy]	abs. flux & error [mJy]
2455188.7545	24.76	12.66	25.01	12.72
2455188.7650	30.12	15.51	30.42	15.58
2455188.7755	23.75	15.33	23.99	15.37
2455188.7859	18.27	14.13	18.45	14.16
2455188.7964	24.45	14.94	24.69	14.99
2455188.8069	21.03	15.99	21.24	16.02
2455188.8174	18.72	15.44	18.91	15.47
2455188.8279	27.61	15.00	27.89	15.06
2455188.8384	35.60	13.82	35.96	13.94
2455188.8489	31.83	12.85	32.16	12.95
2455188.8593	34.21	11.94	34.55	12.06
2455188.8698	32.95	12.02	33.28	12.13
2455368.3739	37.54	7.44	37.92	7.67
2455368.3837	31.83	8.60	32.15	8.75
2455368.3935	34.26	7.23	34.61	7.43
2455368.4033	40.41	4.82	40.82	5.23
2455368.4131	35.11	7.58	35.46	7.78
2455368.4229	28.59	7.91	28.88	8.03
2455368.4327	24.13	8.30	24.37	8.39
2455368.4425	24.37	7.48	24.62	7.58
2455368.4522	22.05	8.87	22.27	8.94
2455368.4620	32.03	6.84	32.35	7.03
2455368.4718	33.66	7.97	34.00	8.15
2455368.4816	21.51	11.32	21.73	11.37
2455368.4914	29.50	10.45	29.79	10.55
2455368.5012	27.60	8.83	27.88	8.94
2455368.5110	20.43	9.93	20.64	9.99
2455368.5208	27.05	9.48	27.32	9.57
2455368.5306	20.66	8.31	20.87	8.37

Table A.9: Herschel-PACS 3-band observations from 2010 Jun 21. The times are observation mid-times in the Herschel reference frame.

mid-time obs. epoch	band	in-band flux & error [mJy]	in-band flux & error [mJy]	$\lambda_{ref}$ [ $\mu\text{m}$ ]	abs. flux & error [mJy]	abs. flux & error [mJy]	OBSIDs
2455369.45202	blue	13.79	2.30	70.0	13.8	2.4	1342198903/904
2455369.46740	green	14.49	3.50	100.0	14.8	3.6	1342198905/906
2455369.45933	red	31.48	5.26	160.0	31.8	5.5	1342198903/904/905/906